

## ABSTRACT

Title of Thesis: AN OBSERVER FOR ESTIMATING  
TRANSLATIONAL VELOCITY  
FROM OPTIC FLOW AND RADAR

Steven Anthony Gerardi, Master of Science, 2011

Thesis directed by: Professor J. Sean Humbert  
Department of Aerospace Engineering

This thesis presents the development of a discrete time observer for estimating state information from optic flow and radar measurements. It is shown that estimates of translational and rotational speed can be extracted using a least squares inversion for wide fields of view or, with the addition of a Kalman Filter, for small fields of view. The approach is demonstrated in a simulated three dimensional urban environment on an autonomous quadrotor micro-air-vehicle (MAV). A state feedback control scheme is designed, whereby the gains are found via static  $H_\infty$ , and implemented to allow trajectory following. The proposed state estimation scheme and feedback method are shown to be sufficient for enabling autonomous navigation of an MAV. The resulting methodology has the advantages of computational speed and simplicity, both of which are imperative for implementation on MAVs due to stringent size, weight, and power requirements.

AN OBSERVER FOR ESTIMATING TRANSLATIONAL  
VELOCITY FROM OPTIC FLOW AND RADAR

by

Steven Anthony Gerardi

Thesis submitted to the Faculty of the Graduate School of the  
University of Maryland, College Park in partial fulfillment  
of the requirements for the degree of  
Master of Science  
2011

Advisory Committee:  
Professor J. Sean Humbert, Chair/Advisor  
Professor Robert Sanner  
Professor Roberto Celi

© Copyright by  
Steven Anthony Gerardi  
2011

## Acknowledgments

First and foremost I'd like to thank my advisor, Professor Sean Humbert for providing me with the opportunity to work in his lab on challenging and interesting projects. It has been a pleasure working with you in both the classroom and laboratory. I would also like to thank my undergraduate advisor Professor Darryll Pines as well as Evan Ulrich for taking me on when I was but a mere Sophomore to work alongside Evan on the mechanical maple seed research. I learned a great deal from you both and truly appreciate the opportunity to work on such a cool project.

Next, I would like to give a big shout out to everyone in the AVL. Joe, you were a tremendous influence on everyone in the lab, both academically and socially. We all appreciated your willingness to discuss everything from LabVIEW code to the proper execution of the Turtle Dance. Thanks to everyone else in the AVL for your support and overall coolness: Greg, Mac, Renee, Badri, Imraan, Kedar, Nick and Doug. Derek, I should also thank you for your incessant bombardment of encouragement, by which I mean I enjoyed our friendly banter and would like to inform you, I win.

Thanks to my former roommates Ryan and Joey, you guys are totes awes. To the rest of the CP gang – Ben, Anthony, Am, Kyle, Jess, Andy, and Heather – you guys were alright. Which reminds me, 8900, a.k.a. “Squalour,” deserves a shout out of its own. You will be missed.

Last but not least, I'd like to give a big Thank You! to my family: Mom, Dad, Craig, Renée, and Eric. I wouldn't be here without everything you have given me.

# Table of Contents

List of Tables	iv
List of Figures	v
Nomenclature	vii
1 Introduction	1
1.1 Optic Flow based Navigation in Robotics . . . . .	4
1.2 Thesis Contributions and Organization . . . . .	6
2 Micro Air Vehicle Sensing and Dynamics	9
2.1 Optic Flow . . . . .	9
2.2 Radar . . . . .	11
2.3 Vehicle Dynamics . . . . .	12
3 State Estimation	16
3.1 Static Estimation . . . . .	17
3.1.1 Measurement Model . . . . .	18
3.1.1.1 Yaw Plane Optic Flow and Radar . . . . .	19
3.1.1.2 Spherical Optic Flow and Radar . . . . .	21
3.1.2 Least Squares Inversion . . . . .	23
3.2 Dynamic Estimation . . . . .	24
3.3 Noise Characterization . . . . .	28
4 Navigation	31
4.1 Gain Matrix Selection . . . . .	33
4.2 State Feedback . . . . .	39
5 MAV Simulation Results	42
5.1 Methodology . . . . .	42
5.2 Experimental Results . . . . .	45
5.2.1 Measurement Noise Characterization . . . . .	45
5.2.2 Experiment 1: Full Lower Hemisphere . . . . .	48
5.2.3 Experiment 2: $18^\circ \times 18^\circ$ . . . . .	53
5.3 Discussion . . . . .	57
6 Conclusions and Future Work	64
6.1 Summary . . . . .	64
6.2 Limitations of Applicability . . . . .	65
6.3 Future Work . . . . .	67
A Measurement Noise Derivations	69
Bibliography	72

## List of Tables

2.1	Quadrotor Parameter Values . . . . .	14
4.1	$H_\infty$ Inner Loop and Outer Loop Gains . . . . .	39
5.1	Standard Deviations for Velocity and Rate Estimates . . . . .	53
5.2	Standard Deviations for Velocity and Rate Estimates: Experiments 3 and 4. . . . .	59
5.3	Average Frobenius Norm for Velocity and Rate Estimates . . . . .	63

## List of Figures

2.1	Geometry of imaging surface for spherical optic flow. (A) Azimuth and elevation angle definitions. (B) Optic flow components $\dot{Q}^\beta$ and $\dot{Q}^\gamma$ .	10
2.2	X-UFO Quadrotor.	12
2.3	Quadrotor axes definitions.	13
3.1	Quadrotor axes definitions in tunnel environment when constrained to 3 DOF with ring constrained optic flow and radar.	19
4.1	Desired trajectories for quadrotor to follow.	32
4.2	Control Loop Structure.	33
4.3	System Description.	34
4.4	Equivalent Control Loop Structure.	40
5.1	3-D simulation environment.	43
5.2	Spherical optic flow simulation process diagram.	44
5.3	Cross sectional view of quadrotor and angular spacing of elevation angle $\beta$ .	44
5.4	Optic Flow and Radar Configuration with a Field of View of the full lower hemisphere. Screen shots from AVLsim of (A) a top view and (B) a rear view.	48
5.5	Estimated vs. actual speeds and rates with measurements taken over the full lower hemisphere of the viewing surface and estimates found using only the least squares estimation scheme.	50
5.6	Estimated vs. actual speeds and rates with measurements taken over the full lower hemisphere of the viewing surface and estimates found using a low pass filter on the least squares estimates.	51
5.7	Estimated vs. actual speeds and rates with measurements taken over the full lower hemisphere of the viewing surface and estimates found using the Kalman filtering scheme.	52
5.8	Optic Flow and Radar Configuration with a Field of View of $18^\circ \times 18^\circ$ . (A) Sketch of radar and optic flow sensor capture volume. (B) Screen shot of quadrotor in AVLsim.	54
5.9	Estimated vs. actual speeds and rates with sensor FOV of $18^\circ \times 18^\circ$ using only the least squares estimation scheme.	55
5.10	Estimated vs. actual speeds and rates with sensor FOV of $18^\circ \times 18^\circ$ using the Kalman filtering scheme.	56
5.11	Estimated vs. actual speeds and rates with sensor FOV of $90^\circ \times 90^\circ$ and estimates found using only the least squares estimation scheme.	60
5.12	Estimated vs. actual speeds and rates with sensor FOV of $90^\circ \times 90^\circ$ and estimates found using a low pass filter on the least squares estimates.	61
5.13	Estimated vs. actual speeds and rates with sensor FOV of $54^\circ \times 54^\circ$ and estimates found using only the least squares estimation scheme.	62

5.14 Estimated vs. actual speeds and rates with sensor FOV of  $54^\circ \times 54^\circ$  and estimates found using a low pass filter on the least squares estimates. . . . . 63

## Nomenclature

$x$	Inertial x position
$y$	Inertial y position
$z$	Inertial z position
$u$	Body-fixed longitudinal velocity
$v$	Body-fixed lateral velocity
$w$	Body-fixed heave velocity
$p$	Body-fixed roll rate
$q$	Body-fixed pitch rate
$r$	Body-fixed yaw rate
$\phi$	Roll angle
$\theta$	Pitch angle
$\psi$	Yaw angle
$\delta_{lat}$	Vehicle lateral input
$\delta_{lon}$	Vehicle longitudinal input
$\delta_{thr}$	Vehicle throttle input
$\delta_{yaw}$	Vehicle yaw input
$\mathbf{x}$	State vector
$\mathbf{u}$	Control input vector
$\beta$	Body referred elevation angle
$\gamma$	Body referred azimuth angle
$n$	Number of states
$N$	Number of measurement nodes
$\dot{\mathbf{Q}}$	Optic flow
$\boldsymbol{\nu}$	Optic flow measurement noise vector
$\mu$	Nearness function
$\boldsymbol{\eta}$	Nearness measurement noise vector
DOF	Degrees of Freedom
FOV	Field of View
GPS	Global Positioning System
IMU	Inertial Measurement Unit
KF	Kalman Filter
LPF	Low Pass Filter
LQR	Linear Quadratic Regulator
LTI	Linear Time Invariant
LS	Least Squares Estimator
MAV	Micro Air Vehicle
UAV	Unmanned Air Vehicle
WFI	Wide Field Integration

## Chapter 1

### Introduction

Unmanned air vehicles (UAVs) are a well established class of aircraft which have been in use for several decades. UAVs carry a variety of sensors capable of determining the vehicles' pose and velocity to enable a level of autonomy which includes stability control, trajectory tracking, and GPS-based waypoint navigation. However, these vehicles are designed for missions at high altitudes and are thus unable to navigate unmapped obstacles such as buildings, trees, or telephone wires. In recent years, an emphasis has been placed on the development of micro air vehicles (MAVs), a miniaturized class of UAVs whose mission profiles typically include navigating close to the ground in unmapped, cluttered outdoor or indoor environments. These vehicles require more precise sensing and control than typical UAVs to safely navigate the cluttered environments. The ability for a vehicle to autonomously estimate egomotion and proximity to obstacles is considered an advanced capability, even for large vehicles. MAVs are very small platforms, typically on the order of several hundred grams or less, so they are limited to carrying small, low weight sensors with low power and processing requirements, thus severely restricting the type of sensors and control algorithms which can be implemented on-board. As a result, the investigation of novel sensing techniques is necessary to advance MAV technology.

Recent advancements in radar technology have allowed researchers to design miniaturized radar sensors which may be implemented on MAVs. Scientists at the University of Michigan are currently developing a radar sensor with a mass of 5 grams and peak power of 200 mW [1, 2]. This thesis investigates the combination of Michigan’s radar sensor and an optical camera for state estimation and control of small autonomous vehicles. The focus of this thesis is to obtain translational velocity  $(u,v,w)$  and angular rate  $(p,q,r)$  estimates of sufficient accuracy to be used in feedback control for aircraft stabilization and obstacle avoidance. Unfortunately, accurate translational velocity measurements can be difficult to obtain, particularly for MAVs. Inertial measurement units (IMUs), which contain gyros and accelerometers, are the state-of-the-art in velocity and rate estimation due to their low weight and power requirements. While gyro measurements tend to show some bias, accelerometer data, which can provide velocity estimates, experience random walk behavior stemming from integrating accelerometer noise and resulting in highly biased estimates. In general, inertial measurement is much more capable of determining attitude motion than translational motion. As a result, vehicles using IMUs typically benefit from the addition of sensors such as GPS or vision-based systems in order to provide accurate knowledge of translational motion. In this thesis, emphasis is placed on obtaining accurate translational velocity estimates without the use of GPS or IMU sensors. Rather, these estimates are obtained using the combination of an omni-directional visual sensor and a radar sensor.

Naturally, vision is an appealing technique for providing a thorough knowledge of an environment. Several machine vision approaches have been investigated [3, 4,

5, 6, 7], but many of these techniques prove to be computationally expensive and physically cumbersome. Vision-based sensors typically require robust estimation schemes such as the extended Kalman Filter (EKF) [4], the unscented Kalman Filter (UKF) [5], or sigma point Kalman Filters [7], which are non-linear estimation techniques that lead to computational complexity and more physically cumbersome systems. As result, the vehicles which utilize these vision methods tend to be much larger than a typical MAV just to be able to carry the sensors and accompanying hardware to implement machine vision.

However, one visual based method for detecting speed and proximity to obstacles which has proven to be viable for implementation on MAVs is optic flow. Derived from the visual perception of flying insects, optic flow is the characteristic patterns of visual motion which form on the retinas of insects as they move about an environment. These patterns are a function of relative speed and relative proximity of the insect to obstacles in the surroundings.

Scientists are able to mimic the way insects compute optic flow using man made cameras and algorithms which monitor the changes in luminosity patterns with time. Due to the small size, weight and computation power needed for optic flow sensors, as well as the ample information they can extract from images of the environment, optic flow is an ideal candidate for unmanned vehicles.

## 1.1 Optic Flow based Navigation in Robotics

Since optic flow was first recognized as a feasible sensing method for MAVs, many researchers have investigated different schemes for utilizing optic flow in MAV control and navigation. One of the earliest and most widely used control strategy is the “balance strategy,” which attempts to center the vehicle between obstacles by equalizing optic flow measurements on the left and right sides of the vehicle [8]. Several studies investigate the application of this centering scheme to regulate the velocity of a vehicle travelling through tunnels of various widths [9, 10, 11, 12, 13, 14, 15]. While these methods provide navigational cues for obstacle avoidance, they ignore the problem of accurate state estimation for use with traditional feedback control approaches.

In pursuit of a more formal approach to allow the use of conventional navigation and control techniques, many researchers have investigated the use of optic flow for state estimation [16, 17, 18, 19, 20, 21, 22, 23, 24]. Some studies have explored extracting total velocity estimates from optic flow but ignored the problem of finding estimates for the directional velocities [17, 16]. Many studies use an extended Kalman Filter (EKF) with the non-linear optic flow equations forming the measurement model [16, 17, 18, 4]. Not only do these solutions require a linearization step during each state estimate step, but some require the addition of an IMU [18] or a feature detection step in order to reduce the noise inherent in the optic flow measurements [16, 17, 4]. While these schemes can provide decent estimates, since they use dynamic filtering strategies to clean up optic flow estimates they can be

quite computationally expensive and thus difficult to implement on an MAV. More recently, some researchers have investigated Wide Field Integration (WFI) of optic flow for state estimation [19, 20, 21, 22, 23]. WFI provides excellent state estimates with very low computation and power requirements. However, WFI schemes require the development of weighting patterns which map optic flow data from a spatially distributed sensor array to actuator commands. The development of these weighting patterns require an assumed structure for a vehicles' immediate surroundings. While the environment model assumptions made in [23] are typically sufficient, this work seeks to use optic flow measurements for state estimation without making any assumptions about the environment and using sensors with a smaller field of view.

The goal of this work is to combine raw optic flow measurements with data collected from a radar sensor to accurately estimate translational and rotational velocity. Optic flow is a relative measure of speed over proximity. Therefore, if accurate proximity measurements can be acquired and compared with optic flow estimates, then more accurate knowledge of velocity can be obtained. Franz et. al. [24] investigated a method for obtaining translational and rotational velocity estimates from optic flow and prior knowledge of an environment. Franz sent a rotating laser scanner through an office environment along several prescribed paths to simulate typical motion patterns of an autonomous robot. The laser scanner was used to collect distance statistics which include properties of both the environment and of specific movement patterns of a robot. The distance measurements provide an average nearness and covariance which were supplied to a "robot" equipped with a vision sensor for computing optic flow. The robot used a static estimation scheme derived

from least squares to estimate egomotion from the optic flow measurements and pre-recorded distance statistics. The results obtained from Franz's experiments revealed that accurate estimates of rotational velocity could be obtained because rotational optic flow has no dependence on distance statistics. However, since translational optic flow is highly dependent on distance, the translational velocity estimates obtained by Franz were much less accurate and degraded quickly against changing scenes and simultaneous rotation. The results obtained by Franz validates the proof of concept for his proposed egomotion estimation scheme. However, since it relies so heavily on prior knowledge of an environment and an assumed vehicle trajectory, it is infeasible for implementation on an autonomous MAV. Thus, this work improves on the scheme proposed by Franz by adding an active distance measurement sensor, such as a miniaturized radar sensor, to an autonomous 6 DOF robot in order to provide proximity measurements captured simultaneously with optic flow measurements so that better speed information can be extracted. This would allow the vehicle to traverse along any path without prior knowledge of the environment and still obtain accurate translational and rotational velocity measurements.

## 1.2 Thesis Contributions and Organization

While optic flow has proven to be a viable source of information for MAV navigation, this work presents one alternative implementation of obtaining state information from optic flow. The goal of this thesis is to develop an estimation scheme which can be applied to a 6 DOF autonomous MAV with on-board radar to obtain

accurate velocity information sufficient for feedback control. To achieve this goal, experiments must be conducted to determine a sufficient sensor arrangement which will yield accurate velocity estimates while still maintaining a realizable hardware configuration. The proposed solution builds on the estimation scheme investigated in [24] by including a discrete time Kalman Filter to reduce noise in the velocity and rate estimates resulting from sensor arrangements with small fields of view. Rather than using a non-linear Kalman Filter to clean up optic flow estimates as in many previous studies, the linear Kalman Filter implemented in this work improves estimates for the six velocity and rate states  $u, v, w, p, q, r$  obtained from the integration of optic flow estimates and radar measurements via least squares estimation. The advantage of this implementation of the Kalman Filter is computational simplicity because fewer states are filtered and there is no need for a linearization step during each state estimation step. Finally, a feedback control scheme, which is robust to noise in state estimates and allows a 6 DOF vehicle to navigate a 3D urban environment, is developed.

This thesis is organized as follows. Chapter 2 presents a discussion on the optic flow and radar sensors used for state estimation as well as a description of the vehicle testbed used to validate the estimation and control methods presented in this thesis. Chapter 3 presents the various state estimation schemes investigated for this research, including both static and dynamic estimators employing spherical optic flow and radar. Chapter 4 describes the static  $H_\infty$  feedback control scheme implemented to regulate position, orientation and velocity using state estimates computed from the methods presented in Chapter 3. Chapter 5 presents results

obtained from simulation of the estimation and control schemes discussed in the previous chapters. Finally, Chapter 6 summarizes the findings of this research and discusses some directions for future work.

## Chapter 2

### Micro Air Vehicle Sensing and Dynamics

This chapter presents the sensors used for state estimation in this study. The theory associated with optic flow is discussed and mathematical models are presented. The radar sensors are described and the vehicle testbed and dynamics are discussed.

#### 2.1 Optic Flow

Optic flow is the apparent visual motion experienced by an observer when moving through an imaged environment. True optic flow is the vector field describing the relative velocities of points within the projected image over the viewing surface, e.g. the retina of an insect. This velocity field is defined by the translational and rotational motion, as well as the relative proximity of the observer to objects in the surrounding environment. The optic flow pattern  $\dot{\mathbf{Q}}$  on a spherical surface can be expressed mathematically [25] as

$$\dot{\mathbf{Q}} = \boldsymbol{\omega} \times \mathbf{r} + \mu[\mathbf{v} - \langle \mathbf{v}, \mathbf{r} \rangle \mathbf{r}] \quad (2.1)$$

where  $\boldsymbol{\omega} = [p, q, r]^T$  is the angular velocity of the vantage point,  $\mathbf{v} = [u, v, w]^T$  is the translational velocity of the vantage point, and  $\mu$  is the nearness function,

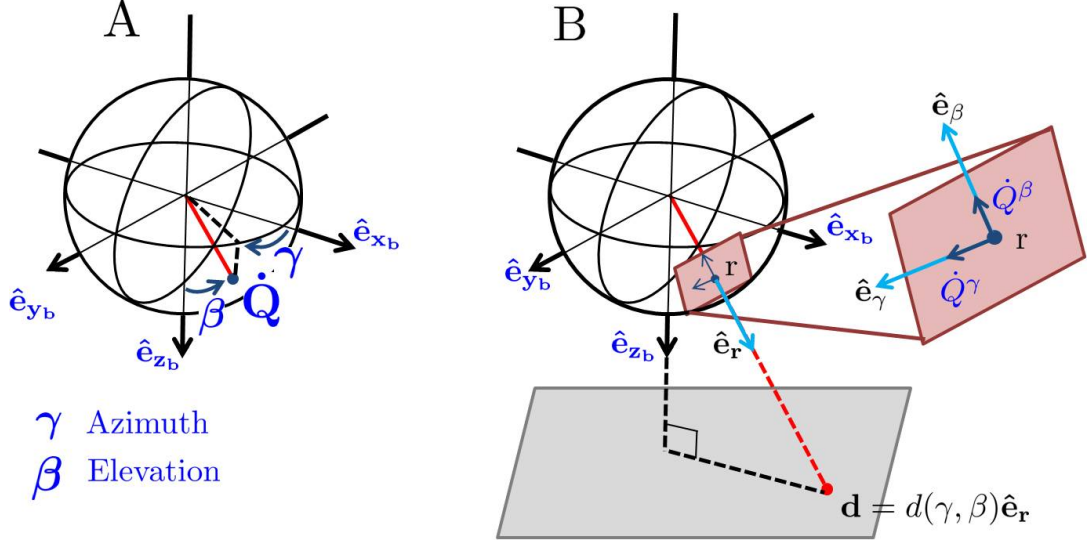


Figure 2.1: Geometry of imaging surface for spherical optic flow. (A) Azimuth and elevation angle definitions. (B) Optic flow components  $\dot{Q}^\beta$  and  $\dot{Q}^\gamma$ .

which represents the distribution of objects in the surrounding environment. The nearness function is defined as the inverse of the distance  $d(\gamma, \beta)$  from the observer to an object in the environment through a point on the imaging surface  $\mathbf{r}(\gamma, \beta)$  at a particular viewing angle of azimuth  $\gamma \in [0, 2\pi]$  and elevation  $\beta \in [0, \pi]$ . Thus  $\mu(\gamma, \beta) = \frac{1}{d(\gamma, \beta)}$  where  $d(\gamma, \beta) \in [0, \infty)$ . Figure 2.1 illustrates the optic flow pattern from Eqn (2.1) can be broken down into components of azimuth and elevation:

$$\dot{\mathbf{Q}} = \dot{Q}^\gamma \hat{e}_\gamma + \dot{Q}^\beta \hat{e}_\beta \quad (2.2)$$

where

$$\begin{aligned} \dot{Q}^\gamma &= p \cos \beta \cos \gamma + q \cos \beta \sin \gamma - r \sin \beta + \mu(u \sin \gamma - v \cos \gamma) \\ \dot{Q}^\beta &= p \sin \gamma - q \cos \gamma + \mu(-u \cos \beta \cos \gamma - v \cos \beta \sin \gamma + w \sin \beta). \end{aligned} \quad (2.3)$$

In robotic applications, optic flow is measured as either 1-D flow (either  $\dot{Q}^\gamma$  or  $\dot{Q}^\beta$ ) or 2-D flow (both  $\dot{Q}^\gamma$  and  $\dot{Q}^\beta$ ). In the work presented in this research, 2-D optic flow is assumed.

## 2.2 Radar

Radar is a valuable source for collecting environment knowledge. It is a well established sensor on both manned and unmanned aircraft. Synthetic Aperature Radar (SAR) is a common form of radar found on aircraft. This type of radar is used by repeatedly emitting pulses of radio waves with wavelengths between a meter to just a few millimeters from a single beam-forming antenna. The returning, or echo, waveforms recieved in succession as the vehicle translates are stored and post-processed together to resolve an image of the targeted region. While common on UAVs, these radar systems are typically on the order of 50 pounds or more — impossible sizes for a MAV. The Radiation Lab at the University of Michigan is currently working on minaturizing radar sensors suitable for use on MAV platforms. The radar being developed at Michigan is a 215 GHz electronically-scanned radar with a horizontal field of view of 50 degrees, with 2-degree resolution, and a vertical field of view of 30 degrees. The range resolution is 25 cm, which is determined by the chirp bandwidth of the system, while the range of the system is approximately 200 meters, given the noise levels chosen [1, 2].

## 2.3 Vehicle Dynamics

The vehicle used to test the state estimation and control algorithms derived in this study is an X-UFO Quadrotor MAV made by Ascending Technologies GmbH. The 6 DOF vehicle, shown in Figs. 2.2 and 2.3, has an overall diameter of 40 cm, an overall mass of 505 g, and rotor diameter of 20 cm. A linearized flight dynamics model was obtained by Gremillion in [26]. The kinematics and dynamics are linearized about forward flight with  $u_{ref} = 1$  m/s. For simulation, the full

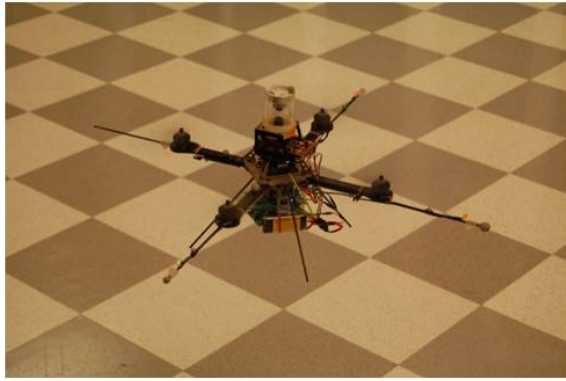


Figure 2.2: X-UFO Quadrotor.

nonlinear kinematic equations are used. The equations of motion are

$$\begin{aligned}
 \dot{u} &= X_u u + X_\theta \theta \\
 \dot{v} &= Y_v v - u_{ref} r + Y_\phi \phi \\
 \dot{w} &= Z_w w + u_{ref} q + Z_{thr} \delta_{thr} \\
 \dot{p} &= L_p p + L_\phi \phi + L_{lat} \delta_{lat} \\
 \dot{q} &= M_q q + M_\theta \theta + M_{lon} \delta_{lon} \\
 \dot{r} &= N_r r + N_{yaw} \delta_{yaw} \\
 \dot{\phi} &= \Phi_p p + \Phi_{lat} \delta_{lat} \\
 \dot{\theta} &= \Theta_q q + \Theta_{lon} \delta_{lon} \\
 \dot{\psi} &= \Psi_r r + \Psi_{yaw} \delta_{yaw}
 \end{aligned} \tag{2.4}$$

The actuator saturation limits are:  $|\delta_{lat}| \leq 1$ ,  $|\delta_{lon}| \leq 1$ ,  $|\delta_{yaw}| \leq 1$ ,  $|\delta_{thr}| \leq 1$ . The

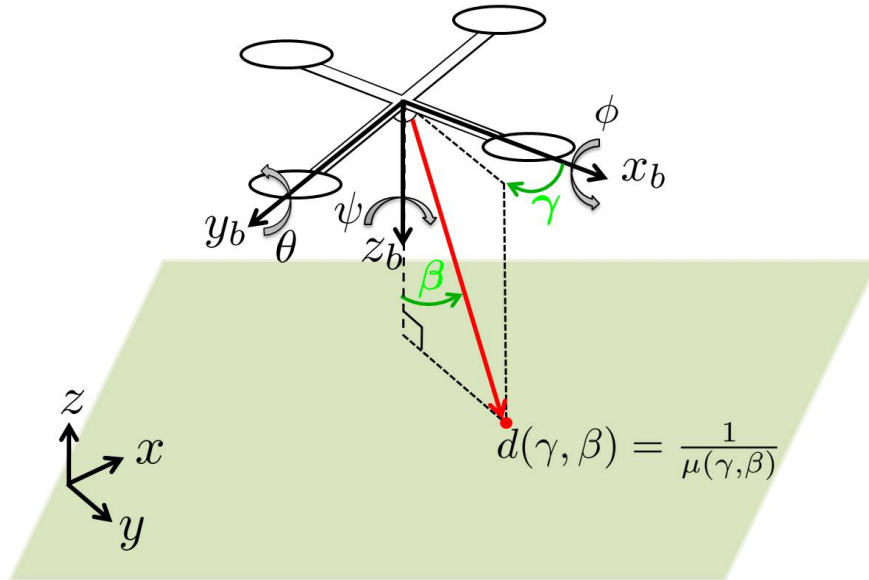


Figure 2.3: Quadrotor axes definitions.

Table 2.1: Quadrotor Parameter Values

Parameter	Value	Parameter	Value
$X_u$	-0.27996	$\Phi_p$	0.9655
$Y_v$	-0.22566	$\Theta_q$	0.9634
$Z_w$	-1.2991	$\Psi_r$	0.6748
$L_p$	-2.5110	$Z_{thr}$	-39.282
$M_q$	-2.4467	$L_{lat}$	11.468
$N_r$	-0.4948	$M_{lon}$	9.5711
$X_\theta$	-10.067	$N_{yaw}$	3.5647
$Y_\phi$	9.8648	$\Phi_{lat}$	0.0744
$L_\phi$	-21.358	$\Theta_{lon}$	0.0594
$M_\theta$	-18.664	$\Psi_{yaw}$	0.0397

characteristic stability derivatives are defined in Table 2.1.

For convenience in later chapters, Eqn. (2.4) can be expressed in the typical linear time invariant state space model of the form  $\dot{\mathbf{x}} = A\mathbf{x} + B\mathbf{u}$  where the state vector is given by  $\mathbf{x} = [\phi, \theta, \psi, u, v, w, p, q, r]^T$ , the control input vector is  $\mathbf{u} = [\delta_{lat}, \delta_{lon}, \delta_{thr}, \delta_{yaw}]^T$  and the dynamics and controls matrices are given in (2.5) and (2.6), respectively.

$$A = \begin{bmatrix} 0 & 0 & 0 & 0 & 0 & 0 & \Phi_p & 0 & 0 \\ 0 & 0 & 0 & 0 & 0 & 0 & 0 & \Theta_q & 0 \\ 0 & 0 & 0 & 0 & 0 & 0 & 0 & 0 & \Psi_r \\ 0 & X_\theta & 0 & X_u & 0 & 0 & 0 & 0 & 0 \\ Y_\phi & 0 & 0 & 0 & Y_v & 0 & 0 & 0 & -u_{ref} \\ 0 & 0 & 0 & 0 & 0 & Z_w & 0 & u_{ref} & 0 \\ L_\phi & 0 & 0 & 0 & 0 & 0 & L_p & 0 & 0 \\ 0 & M_\theta & 0 & 0 & 0 & 0 & 0 & M_q & 0 \\ 0 & 0 & 0 & 0 & 0 & 0 & 0 & 0 & N_r \end{bmatrix} \quad (2.5)$$

$$B = \begin{bmatrix} \Phi_{lat} & 0 & 0 & 0 \\ 0 & \Theta_{lon} & 0 & 0 \\ 0 & 0 & 0 & \Psi_{yaw} \\ 0 & 0 & 0 & 0 \\ 0 & 0 & 0 & 0 \\ 0 & 0 & Z_{thr} & 0 \\ L_{lat} & 0 & 0 & 0 \\ 0 & M_{lon} & 0 & 0 \\ 0 & 0 & 0 & N_{yaw} \end{bmatrix} \quad (2.6)$$

## Chapter 3

### State Estimation

This chapter presents strategies for estimating vehicle velocity states using on-board sensor measurements. A simple static least squares estimator which fuses optic flow and radar measurements is developed to estimate translational and rotational velocity. In addition, an implementation of the linear Kalman Filter is derived in order to reduce noise in the least square estimates.

Optic flow is not a quantity which can be measured directly; rather, the value  $\dot{\mathbf{Q}}$  is an estimate of optic flow which is dependent on the luminance incident on the imaging surface. This estimation process, along with sensor noise and contrast and texture variations throughout the surfaces in the environment, introduce error into the optic flow measurements. In addition, the radar proximity measurements are also corrupted by several sources of noise.

Given the noisy measurements available from optic flow and radar, the goal is to obtain rate and velocity information necessary to control an aircraft and permit autonomous navigation of a cluttered environment. In other words, the goal is to find an estimate  $\hat{\mathbf{x}}$  of the state vector  $\mathbf{x}$  given the linear state space model

$$\dot{\mathbf{x}} = A\mathbf{x} + B\mathbf{u} \tag{3.1}$$

$$\mathbf{y} = C\mathbf{x} \tag{3.2}$$

where  $\mathbf{u}$  is the control vector,  $A$  is a linear, time invariant system matrix,  $B$  is a matrix of constant control sensitivity derivatives, and  $C$  is the output equation matrix. The process model, (3.1), for the quadrotor can be found from (2.5) and (2.6).

### 3.1 Static Estimation

In this section, a method of static estimation for determining translational and rotational velocity from noisy measurements is presented. In optic flow estimation, the combined effect of the various uncertainties have been modelled in [27, 28] as zero mean white Gaussian noise. Thus the optic flow measurement is expressed as

$$\dot{\hat{\mathbf{Q}}} = \dot{\mathbf{Q}} + \boldsymbol{\nu}, \quad (3.3)$$

where  $\dot{\hat{\mathbf{Q}}}$  is the optic flow measurement, and  $\boldsymbol{\nu}$  is noise assumed to be zero mean, white, and uncorrelated with itself at different viewing angles and directions. Therefore, if the following vectors are defined:

$$\boldsymbol{\nu}_\gamma = \begin{bmatrix} \nu_\gamma(\gamma_1, \beta_1) \\ \nu_\gamma(\gamma_2, \beta_2) \\ \vdots \\ \nu_\gamma(\gamma_N, \beta_N) \end{bmatrix}, \quad \boldsymbol{\nu}_\beta = \begin{bmatrix} \nu_\beta(\gamma_1, \beta_1) \\ \nu_\beta(\gamma_2, \beta_2) \\ \vdots \\ \nu_\beta(\gamma_N, \beta_N) \end{bmatrix}$$

where  $\nu_\gamma$  is the noise on the optic flow measurement in the azimuthal direction  $\dot{\hat{Q}}^\gamma$ ,  $\nu_\beta$  is the noise on the optic flow measurement in the elevation direction  $\dot{\hat{Q}}^\beta$ ,

and  $N$  is the number of optic flow measurement nodes, then  $E[\boldsymbol{\nu}_\gamma \boldsymbol{\nu}_\beta^\top] = 0$  and  $E[\boldsymbol{\nu}_\gamma \boldsymbol{\nu}_\gamma^\top] = \sigma_\nu^2 I_{N \times N}$ . It is also assumed that the noise covariance is identical at each measurement node and in both directions  $E[\boldsymbol{\nu}_\gamma \boldsymbol{\nu}_\gamma^\top] = E[\boldsymbol{\nu}_\beta \boldsymbol{\nu}_\beta^\top]$ . The radar distance measurements, too, are corrupted by noise, thus,

$$\tilde{\boldsymbol{\mu}} = \boldsymbol{\mu} + \boldsymbol{\eta}. \quad (3.4)$$

where  $\tilde{\boldsymbol{\mu}}$  is the nearness measurement, and  $\boldsymbol{\eta}$  is noise assumed to be zero mean, white, and uncorrelated with itself at different viewing angles. If the following vector is defined

$$\boldsymbol{\eta} = \begin{bmatrix} \eta(\gamma_1, \beta_1) \\ \eta(\gamma_2, \beta_2) \\ \vdots \\ \eta(\gamma_N, \beta_N) \end{bmatrix},$$

then  $E[\boldsymbol{\eta} \boldsymbol{\eta}^\top] = \sigma_\eta^2 I_{N \times N}$ .

### 3.1.1 Measurement Model

In state estimation, it is required that a set of measurements,  $\tilde{\mathbf{z}}$ , which are dependent on the states  $\mathbf{x}$  and thus provide knowledge of the system dynamics, can be obtained. Furthermore, for simplicity, we can impart the restriction that the measurements be linearly related to the states. The equation which relates  $\mathbf{x}$  to  $\tilde{\mathbf{z}}$  is expressed as:

$$\tilde{\mathbf{z}} = H\mathbf{x} + \mathbf{v} \quad (3.5)$$

where  $H$  is the linear transformation from  $\mathbf{x}$  to  $\tilde{\mathbf{z}}$  and  $\mathbf{v}$  is a vector of measurement errors. In this section, measurement models for static estimation are developed for two cases. First, the case of 1-D ring constrained optic flow and radar is examined. This case is applicable to the quadrotor vehicle when constrained to 3 DOF as in Figure 3.1. Next, the case of spherical optic flow and radar, which is applicable to 6 DOF vehicles, is presented.

### 3.1.1.1 Yaw Plane Optic Flow and Radar

We first consider the case of 1-D optic flow restricted to the yaw plane. This measurement domain, defined as a ring of azimuthal measurements ( $\dot{Q}^\gamma$ ), is applicable to the quadrotor presented in Fig. 3.1 which is restricted to forward motion, lateral motion and yaw rotation only, as in [21]. The simplified optic flow model which relates to this case is presented here and is written without subscripts and

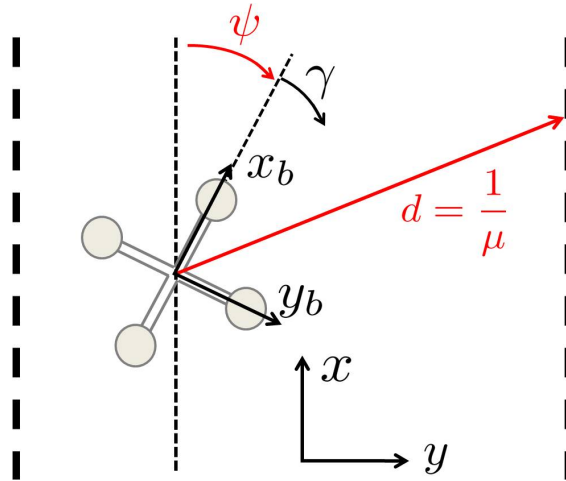


Figure 3.1: Quadrotor axes definitions in tunnel environment when constrained to 3 DOF with ring constrained optic flow and radar.

superscripts for simplicity:

$$\dot{Q} = -r + \mu(u \sin \gamma - v \cos \gamma). \quad (3.6)$$

The observation equation is then obtained from Eqns. (3.6), (3.3) and (3.4). If  $N$  discrete optic flow and radar measurements are taken along the yaw plane, the observation equations are written as

$$\begin{aligned} \dot{Q}_1 &= -r + (\mu_1 + \eta_1)(u \sin \gamma_1 - v \cos \gamma_1) + \nu_1 \\ \dot{Q}_2 &= -r + (\mu_2 + \eta_2)(u \sin \gamma_2 - v \cos \gamma_2) + \nu_2 \\ &\vdots \\ \dot{Q}_N &= -r + (\mu_N + \eta_N)(u \sin \gamma_N - v \cos \gamma_N) + \nu_N \end{aligned} \quad (3.7)$$

By allowing  $v_j = \nu_j + \eta_j(u \sin \gamma_j - v \cos \gamma_j)$  for  $j = 1, 2, \dots, N$ , Eqn. (3.7) can take the form of the linear measurement equation shown in Eqn. (3.5) where  $\tilde{\mathbf{z}}$  is the  $N \times 1$  vector of optic flow measurements  $\tilde{\mathbf{z}} = [\dot{Q}_1, \dot{Q}_2, \dots, \dot{Q}_N]^T$ ,  $\mathbf{x}$  is the  $3 \times 1$  vector of angular and translational velocities  $\mathbf{x} = [u, v, r]^T$ ,  $\mathbf{v}$  is the  $N \times 1$  error vector and  $H$  is the  $N \times 3$  matrix given by

$$H = \begin{bmatrix} \mu_1 \sin \gamma_1 & -\mu_1 \cos \gamma_1 & -1 \\ \mu_2 \sin \gamma_2 & -\mu_2 \cos \gamma_2 & -1 \\ \vdots & \vdots & \vdots \\ \mu_N \sin \gamma_N & -\mu_N \cos \gamma_N & -1 \end{bmatrix}. \quad (3.8)$$

Thus, the full observation equation is written as

$$\begin{bmatrix} \dot{\tilde{Q}}_1 \\ \dot{\tilde{Q}}_2 \\ \vdots \\ \dot{\tilde{Q}}_N \end{bmatrix} = \begin{bmatrix} \mu_1 \sin \gamma_1 & -\mu_1 \cos \gamma_1 & -1 \\ \mu_2 \sin \gamma_2 & -\mu_2 \cos \gamma_2 & -1 \\ \vdots & \vdots & \vdots \\ \mu_N \sin \gamma_N & -\mu_N \cos \gamma_N & -1 \end{bmatrix} \begin{bmatrix} u \\ v \\ r \end{bmatrix} + \begin{bmatrix} \nu_1 + \eta_1(u \sin \gamma_1 - v \cos \gamma_1) \\ \nu_2 + \eta_2(u \sin \gamma_2 - v \cos \gamma_2) \\ \vdots \\ \nu_N + \eta_N(u \sin \gamma_N - v \cos \gamma_N) \end{bmatrix}. \quad (3.9)$$

### 3.1.1.2 Spherical Optic Flow and Radar

Now consider the case of 2-D optic flow measurements taken around the sphere. The observation equation can be obtained in a similar fashion as the planar 1-D case, however the relevant equations are now Eqns. (2.3), (3.3) and (3.4). If optic flow and radar measurements are taken at  $N$  discrete points on the sphere, then the observation equations are written as

$$\begin{aligned} \dot{\tilde{Q}}_j^\gamma &= p \cos \beta_j \cos \gamma_j + q \cos \beta_j \sin \gamma_j - r \sin \beta_j \\ &\quad + (\mu_j(\gamma_j, \beta_j) + \eta_j)(u \sin \gamma_j - v \cos \gamma_j) + \nu_{\gamma,j} \quad \text{for } j = 1, 2, \dots, N \\ \\ \dot{\tilde{Q}}_j^\beta &= p \sin \gamma_j - q \cos \gamma_j + (\mu_j(\gamma_j, \beta_j) + \eta_j)(-u \cos \beta_j \cos \gamma_j \\ &\quad - v \cos \beta_j \sin \gamma_j + w \sin \beta_j) + \nu_{\beta,j} \quad \text{for } j = 1, 2, \dots, N \end{aligned} \quad (3.10)$$

By allowing  $v_{\gamma,j} = \nu_{\gamma,j} + \eta_j(u \sin \gamma_j - v \cos \gamma_j)$  for  $j = 1, 2, \dots, N$  and  $v_{\beta,j} = \nu_{\beta,j} + \eta_j(-u \cos \beta_j \cos \gamma_j - v \cos \beta_j \sin \gamma_j + w \sin \beta_j)$  for  $j = 1, 2, \dots, N$ , Eqn. (3.10) can

take the form of the linear measurement equation shown in Eqn. (3.5) where  $\tilde{\mathbf{z}}$  is the  $2N \times 1$  vector of optic flow measurements

$$\tilde{\mathbf{z}} = [\dot{Q}_1^\gamma, \dot{Q}_2^\gamma, \dots, \dot{Q}_N^\gamma, \dot{Q}_1^\beta, \dot{Q}_2^\beta, \dots, \dot{Q}_N^\beta]^\top,$$

$\mathbf{x}$  is the  $6 \times 1$  vector of angular and translational velocities

$$\mathbf{x} = [u, v, w, p, q, r]^\top,$$

$\mathbf{v}$  is the  $2N \times 1$  error vector

$$\mathbf{v} = \begin{bmatrix} \mathbf{v}_\gamma \\ \mathbf{v}_\beta \end{bmatrix},$$

and  $H$  is the  $2N \times 6$  matrix given by

$$H = \begin{bmatrix} \mu_1 s\gamma_1 & -\mu_1 c\gamma_1 & 0 & c\beta_1 c\gamma_1 & c\beta_1 s\gamma_1 & -s\beta_1 \\ \mu_2 s\gamma_2 & -\mu_2 c\gamma_2 & 0 & c\beta_2 c\gamma_2 & c\beta_2 s\gamma_2 & -s\beta_2 \\ \vdots & \vdots & \vdots & \vdots & \vdots & \vdots \\ \mu_N s\gamma_N & -\mu_N c\gamma_N & 0 & c\beta_N c\gamma_N & c\beta_N s\gamma_N & -s\beta_N \\ -\mu_1 c\beta_1 c\gamma_1 & -\mu_1 c\beta_1 s\gamma_1 & \mu_1 s\beta_1 & s\gamma_1 & -c\gamma_1 & 0 \\ -\mu_2 c\beta_2 c\gamma_2 & -\mu_2 c\beta_2 s\gamma_2 & \mu_2 s\beta_2 & s\gamma_2 & -c\gamma_2 & 0 \\ \vdots & \vdots & \vdots & \vdots & \vdots & \vdots \\ -\mu_N c\beta_N c\gamma_N & -\mu_N c\beta_N s\gamma_N & \mu_N s\beta_N & s\gamma_N & -c\gamma_N & 0 \end{bmatrix} \quad (3.11)$$

where  $s\gamma = \sin \gamma$ ,  $s\beta = \sin \beta$ ,  $c\gamma = \cos \gamma$ , and  $c\beta = \cos \beta$ .

### 3.1.2 Least Squares Inversion

When written as Eqn. (3.5) the problem is posed in the form of a standard static linear estimation problem, in which the solution of an overdetermined, inconsistent set of linear equations is sought. Gauss's principle of least squares solves for  $\hat{\mathbf{x}}$ , the estimate of  $\mathbf{x}$  which minimizes the sum of the square of the residual errors [29]. The residual error is defined as the difference between the measurements and the estimate of the measurements  $\mathbf{e} \equiv \tilde{\mathbf{z}} - \hat{\mathbf{z}}$ , where the estimated measurements are simply defined as  $\hat{\mathbf{z}} = H\hat{\mathbf{x}}$ . Thus, the goal of the least squares method is to solve for  $\hat{\mathbf{x}}$  by minimizing the cost function  $J = \frac{1}{2}\mathbf{e}^T\mathbf{e}$ . With some manipulation,  $J$  can be written as

$$J = J(\hat{\mathbf{x}}) = \frac{1}{2}(\tilde{\mathbf{z}}^T\tilde{\mathbf{z}} - 2\tilde{\mathbf{z}}^T H\hat{\mathbf{x}} + \hat{\mathbf{x}}^T H^T H\hat{\mathbf{x}}). \quad (3.12)$$

To minimize  $J$  with respect to  $\hat{\mathbf{x}}$ , the partial derivative is found and set equal to zero:

$$\begin{aligned} \frac{\partial J}{\partial \hat{\mathbf{x}}} &= -\tilde{\mathbf{z}}^T H + \hat{\mathbf{x}}^T H^T H \\ &= 0. \end{aligned} \quad (3.13)$$

Solving this equation for  $\hat{\mathbf{x}}$  results in

$$\begin{aligned}
 H^T H \hat{\mathbf{x}} &= H^T \tilde{\mathbf{z}} \\
 \hat{\mathbf{x}} &= (H^T H)^{-1} H^T \tilde{\mathbf{z}}.
 \end{aligned}
 \tag{3.14}$$

As long as the number of measurements  $N$  is greater than the number of unknown states  $n$ , and the measurements are linearly independent, i.e.  $H$  is full rank, Eqn. (3.14) provides the optimal static estimates for translational and angular velocities,  $\hat{\mathbf{x}} = [\hat{u}, \hat{v}, \hat{r}]^T$  for the planar case in section 3.1.1.1 and  $\hat{\mathbf{x}} = [\hat{u}, \hat{v}, \hat{w}, \hat{p}, \hat{q}, \hat{r}]^T$  for the spherical case in section 3.1.1.2.

## 3.2 Dynamic Estimation

As will be shown in Chapter 5, the least squares static estimation scheme provides adequate estimates for the complicated case of the 6 DOF quadrotor only when the sensor coverage area has a wide field of view. However, for the sensors selected for this work, it is more practical to implement a sensor arrangement with a much more narrow field of view, which leads to a serious degradation in the accuracy of the state estimates. Thus, it is necessary to develop a sequential estimation scheme which follows the recursive process of prediction and correction in order to filter the noisy state estimates resulting from a small field of view. The Kalman Filter provides the optimal estimation for linear systems subject to Gaussian noise and whose state variables can be described with Gaussian probability distributions. The literature on the Kalman Filter is quite extensive and the full derivation can

be found in sources such as [30, 31]. However, the discrete time Kalman Filter will be described in brief here.

First, assume that both the dynamic model of the vehicle and the measurements are available in the discrete time form, and that both model and measurements are corrupted by noise. The model for this case is given by

$$\mathbf{x}_{k+1} = F_k \mathbf{x}_k + G_k \mathbf{u}_k + \mathbf{w}_k \quad (3.15)$$

$$\tilde{\mathbf{y}}_k = C_k \mathbf{x}_k + \mathbf{v}_k \quad (3.16)$$

where  $\mathbf{x}_k$  is the state vector at time  $k$ ,  $\mathbf{u}_k$  is the input vector, and  $\mathbf{v}_k$  and  $\mathbf{w}_k$  are assumed to be zero-mean Gaussian white-noise processes, i.e. the errors are not correlated forward or backward in time, so

$$E[\mathbf{v}_k \mathbf{v}_j] = \begin{cases} 0 & k \neq j \\ R_k & k = j \end{cases} \quad (3.17)$$

$$E[\mathbf{w}_k \mathbf{w}_j] = \begin{cases} 0 & k \neq j \\ Q_k & k = j \end{cases} \quad (3.18)$$

It is further assumed that  $\mathbf{v}_k$  and  $\mathbf{w}_k$  are uncorrelated, i.e.  $E[\mathbf{v}_k \mathbf{w}_k] = 0$  for all  $k$ . If it turns out the noise sources creating  $\mathbf{w}$  are uncorrelated, then  $Q_k$  will be a diagonal matrix with the diagonal elements given by

$$Q_{k,i} = \sigma_{\mathbf{w},i}^2 \quad (3.19)$$

where  $\sigma_{\mathbf{w},i}$  is the standard deviation of the  $i^{\text{th}}$  element of  $\mathbf{w}$ . Likewise, if the noise sources contributing to  $\mathbf{v}$  are uncorrelated, then  $R_k$  will also be a diagonal matrix with the diagonal elements given by

$$R_{k,i} = \sigma_{\mathbf{v},i}^2 \quad (3.20)$$

where  $\sigma_{\mathbf{v},i}$  is the standard deviation of the  $i^{\text{th}}$  element of  $\mathbf{v}$ . If we also assume the dynamics of the system are modelled as LTI, as we have with the vehicle model presented in Chapter 2, and that the time intervals are equally spaced, i.e.  $t_{k+1} - t_k = T$  for each  $k = 0, 1, \dots$ , then  $F_k$  and  $G_k$  are constant matrices,  $F_k = F$  and  $G_k = G$  found from

$$F = e^{AT} \quad (3.21)$$

$$G = \left[ \int_0^T e^{A\tau} d\tau \right] B. \quad (3.22)$$

Finally, assuming  $C$  from Eqn. (3.2) is constant, then  $C_k = C$  is also constant.

The Kalman Filter is defined by the following iterative process. First, estimates of the initial mean and error covariance matrix are given or assumed:

$$\hat{\mathbf{x}}_0^- = E[\mathbf{x}_0] \quad (3.23)$$

$$P_0^- = E[(\mathbf{x}_0 - \hat{\mathbf{x}}_0^-)(\mathbf{x}_0 - \hat{\mathbf{x}}_0^-)^T]. \quad (3.24)$$

Next, at each time step,  $k$ , the following computations are made.

1. Compute the Kalman Filter Gain,  $L_k$

$$L_k = P_k^- C^T [C P_k^- C^T + R_k]^{-1} \quad (3.25)$$

2. Update the state estimate

$$\hat{\mathbf{x}}_k = \hat{\mathbf{x}}_k^- + L_k [\tilde{\mathbf{y}}_k - C \hat{\mathbf{x}}_k^-] \quad (3.26)$$

3. Update the error covariance

$$P_k = [I - L_k C] P_k^- \quad (3.27)$$

4. Predict the next state estimate

$$\hat{\mathbf{x}}_{k+1}^- = F \hat{\mathbf{x}}_k + G \mathbf{u}_k \quad (3.28)$$

5. Predict the next error covariance matrix

$$P_{k+1}^- = F P_k F + Q_k \quad (3.29)$$

For this work, the Kalman Filter is used to improve the noisy velocity and rate estimates obtained through the least squares method in Eqn. (3.14). Thus, the states to be filtered are  $\hat{\mathbf{x}}_{\mathbf{LS}} = [\hat{u}_{LS}, \hat{v}_{LS}, \hat{w}_{LS}, \hat{p}_{LS}, \hat{q}_{LS}, \hat{r}_{LS}]^T$ . However, as seen in Eqn. (2.4), the velocity and rate estimates are coupled with the roll and pitch

states  $\phi$  and  $\theta$ . As a result, measurements of the roll and pitch angles are necessary for the implementation of the Kalman Filter. Luckily, the X-UFO Quadrotor comes equipped with an avionics package capable of measuring roll and pitch. Now the goal of the Kalman Filter is to find state estimates  $\hat{\mathbf{x}} = [\hat{\phi}, \hat{\theta}, \hat{u}, \hat{v}, \hat{w}, \hat{p}, \hat{q}, \hat{r}]^T$  where the measurement vector is given by the angle measurements from the X-UFO avionics and the least squares state estimates  $\tilde{\mathbf{y}} = [\tilde{\phi}, \tilde{\theta}, \hat{u}_{LS}, \hat{v}_{LS}, \hat{w}_{LS}, \hat{p}_{LS}, \hat{q}_{LS}, \hat{r}_{LS}]^T$ . The  $F$  and  $G$  matrices are found from (3.21) and (3.22) where  $A$  and  $B$  are taken from (2.5) and (2.6) with the columns and rows corresponding to the yaw angle  $\psi$  omitted since the translational and rotational velocities are not coupled with the yaw state. The  $C$  matrix is taken to be the Identity matrix  $C = I_{8 \times 8}$ .

### 3.3 Noise Characterization

The implementation of the Kalman Filter also demands accurate noise characterization to determine values for the covariance matrices  $Q_k$  and  $R_k$ . Accurate characterization of process and measurement noise is arguably one of the most difficult steps in optimal state estimation. In this work, process noise was assumed to be negligible, i.e.  $Q_k \approx 0 \forall k$ . On the other hand, the measurements are assumed to be quite noisy, thus the need for an accurate measurement noise model. The characteristics of  $\mathbf{v}$  were determined empirically, allowing for the development of the matrix  $R_k$ .

Measurement noise is highly dependent on the number of optic flow and radar measurements taken as well as the FOV of the sensors. Ideally, the FOV would

encompass the full spherical viewing area around the MAV. However, the physical implementation of such a set-up would be impractical with the radar sensors used in this work. Realistically, the FOV would encompass the viewing area of only one radar sensor as such a design would be easier to implement. However, as the FOV decreases, the noise increases. Likewise, as the number of measurements within the field of view decreases, the noise increases. But fewer measurements corresponds to less processing, thus quicker computation time and less power consumption, all of which is important for MAV sensing. Thus, the trick is to determine an acceptable hardware configuration and number of measurements without sacrificing the accuracy of estimated state values. For that reason, this thesis investigates several simulated hardware configurations, which will be discussed in Chapter 5. However, for each configuration, a new  $R_k$  matrix must be developed to account for the different measurement parameters.

To determine the values for these matrices, the vehicle was flown through the Fort Benning environment along a representative trajectory which takes about 30 seconds to complete. During the flight, optic flow and radar measurements were taken and  $\hat{\mathbf{x}}_{\mathbf{LS}}$  was computed. If we define the vector  $\mathbf{x}_{\mathbf{a}} = [\phi, \theta, u, v, w, p, q, r]^T$  and recall that the measurement vector  $\tilde{\mathbf{y}}$  is simply a vector of the true state values  $\mathbf{x}_{\mathbf{a}}$  plus white noise,

$$\tilde{\mathbf{y}} = \begin{bmatrix} \tilde{\phi} \\ \tilde{\theta} \\ \hat{\mathbf{x}}_{\mathbf{LS}} \end{bmatrix} = \begin{bmatrix} \phi \\ \theta \\ \mathbf{x}_{\mathbf{v}} \end{bmatrix} + \mathbf{v} = \mathbf{x}_{\mathbf{a}} + \mathbf{v} \quad (3.30)$$

where  $\mathbf{x}_v = [u, v, w, p, q, r]^T$ , it can be shown that

$$R_k = E[\mathbf{v}\mathbf{v}^T] = E[(\tilde{\mathbf{y}} - \mathbf{x}_a)(\tilde{\mathbf{y}} - \mathbf{x}_a)^T]. \quad (3.31)$$

Eqn. (3.31) shows that if the true values of the states are known, the noise covariance matrix  $R_k$  can be found by solving for the covariance of the error between the measurements and the true values. The measurements from the X-UFO avionics were assumed to be near perfect and uncorrelated with the velocity and rate estimates obtained from the least squares estimation method, so  $\sigma_\phi^2 = \sigma_\theta^2 = 0.0001$  and  $R_k$  has the structure

$$R_k = \begin{bmatrix} \sigma_\phi^2 & 0 & 0 \\ 0 & \sigma_\theta^2 & 0 \\ 0 & 0 & \Sigma_{\bar{\mathbf{x}}} \end{bmatrix} \quad (3.32)$$

where  $\bar{\mathbf{x}} = \hat{\mathbf{x}}_{\text{LS}} - \mathbf{x}_v$  with covariance matrix  $\Sigma_{\bar{\mathbf{x}}} = E[\bar{\mathbf{x}}\bar{\mathbf{x}}^T] = E[(\hat{\mathbf{x}}_{\text{LS}} - \mathbf{x}_v)(\hat{\mathbf{x}}_{\text{LS}} - \mathbf{x}_v)^T]$ .

An expression for  $\Sigma_{\bar{\mathbf{x}}}$  is derived in Appendix A, where it is shown that the noise sources contributing to the error in  $\hat{\mathbf{x}}_{\text{LS}}$  may be correlated, and Chapter 5 discusses the values obtained for  $\Sigma_{\bar{\mathbf{x}}}$  for each sensor configuration investigated.

## Chapter 4

### Navigation

While the focus of this research is not to develop a novel navigation and control scheme, it is still necessary to utilize an algorithm for path following and vehicle control in order to demonstrate the ability to use the estimated state values for navigation in a cluttered environment. To that end, this chapter develops a control scheme to allow the quadrotor to autonomously navigate a simulated environment. During the simulations, the quadrotor is provided a path to follow through the environment. Each path is intended to closely resemble a typical trajectory an autonomous UAV may take as it traverses through the cluttered environment. Therefore, the desired trajectories are generated by allowing a quadrotor equipped with WFI optic flow sensors and a control scheme similar to that developed in [23] to autonomously navigate the environment from several different initial conditions  $(x_0, y_0, z_0, \psi_0)$  obtained via Monte Carlo simulation. Figure 4.1 displays the generated trajectories for the vehicle to track.

In order for the vehicle to closely track the desired trajectory while maintaining the desired flight conditions for forward flight at  $u = 1$  m/s a control scheme must be developed. Several control schemes were investigated but ultimately, an inner loop and outer loop structure, as depicted in Fig. 4.2, was chosen, whereby the gains were computed via static  $H_\infty$ .

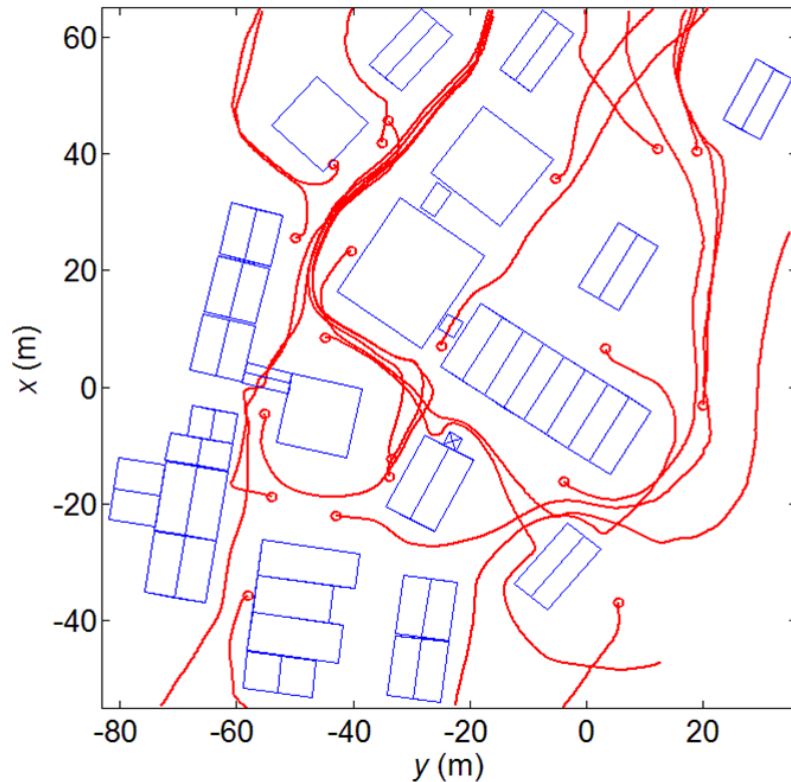


Figure 4.1: Desired trajectories for quadrotor to follow.

As the figure shows, the measurement block includes not only optic flow and radar sensors which provide  $\dot{\mathbf{Q}}$  and  $\boldsymbol{\mu}$  respectively, but also the X-UFO avionics which provide measurements for  $\phi$  and  $\theta$ . These measurements are provided to the least squares estimator and dynamic filter as discussed in Chapter 3. Assuming the initial conditions  $x_0, y_0, z_0, \psi_0$  are known, then the velocity estimates  $\hat{u}, \hat{v}, \hat{w}$  and yaw rate estimate  $\hat{r}$  can be integrated to provide estimates for position and yaw angle,  $\hat{x}, \hat{y}, \hat{z}, \hat{\psi}$ . The inner loop is designed to regulate the measurements  $\phi$  and  $\theta$  and the rate estimates  $\hat{p}, \hat{q}, \hat{r}$ , while the outer loop is designed to track the desired reference states for  $x, y, z$ , and  $\psi$  as well as regulate the velocity estimates  $\hat{u}, \hat{v}, \hat{w}$  to keep the vehicle in the desired flight condition. The following section will discuss

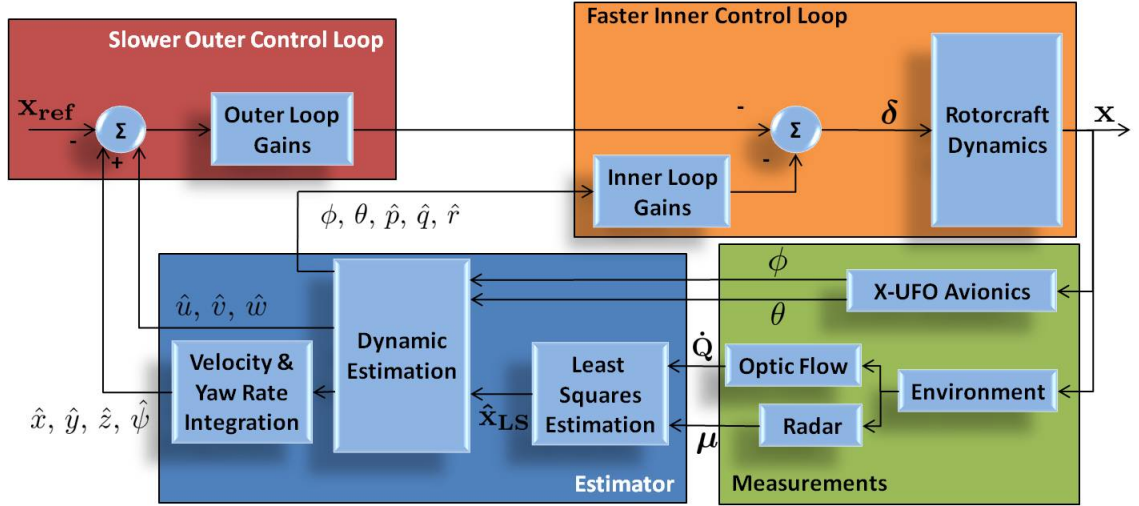


Figure 4.2: Control Loop Structure.

how the gains for the inner and outer loops were chosen.

#### 4.1 Gain Matrix Selection

As mentioned earlier, both the inner and outer loop gains were selected via static  $H_\infty$  output feedback, which is derived in [32]. The static  $H_\infty$  problem statement is as follows: Consider the LTI system shown in Fig. 4.3 given by

$$\begin{aligned}\dot{\mathbf{x}} &= A\mathbf{x} + B\mathbf{u} + D\mathbf{d} \\ \mathbf{y} &= C\mathbf{x}\end{aligned}\tag{4.1}$$

with performance output

$$\|\mathbf{z}\|^2 = \mathbf{x}^T Q \mathbf{x} + \mathbf{u}^T R \mathbf{u},\tag{4.2}$$

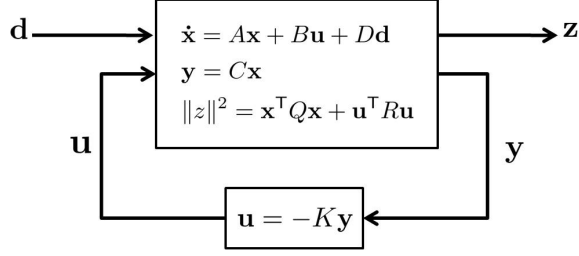


Figure 4.3: System Description.

and control input

$$\mathbf{u} = -K\mathbf{y} = -KC\mathbf{x}, \quad (4.3)$$

where  $\mathbf{d}$  is some exogenous disturbance,  $C$  has full row rank,  $Q \geq 0$  is positive definite and  $R > 0$  is positive semi-definite. The goal is to select gains  $K$  such that the system in Eqn. (4.1) is stable, the performance is satisfied, and the system is robust to disturbances  $d(t)$ .

At this point, a few terms should be defined. The pair  $(A, B)$  is said to be *stabilizable* if there exists a matrix  $K$  such that  $A - BK$  is asymptotically stable. The pair  $(A, C)$  is *detectable* if there exists a matrix  $L$  such that  $A - LC$  is stable. The system in Eqn. (4.1) is *output stabilizable* if there exists a matrix  $K$  such that  $A - BKC$  is stable. Finally, the system  $L_2$  gain is said to be bounded by  $\gamma$  if

$$\frac{\int_0^\infty \|\mathbf{z}(t)\|^2 dt}{\int_0^\infty \|\mathbf{d}(t)\|^2 dt} = \frac{\int_0^\infty (\mathbf{x}^T Q \mathbf{x} + \mathbf{u}^T R \mathbf{u}) dt}{\int_0^\infty (\mathbf{d}^T \mathbf{d}) dt} \leq \gamma^2. \quad (4.4)$$

From this, Gadewadikar [32] states that the goal is to find the matrix  $K$  which

minimizes the cost function

$$J(K, d) = \int_0^{\infty} (\mathbf{x}^T Q \mathbf{x} + \mathbf{u}^T R \mathbf{u} - \gamma^2 \mathbf{d}^T \mathbf{d}) dt.$$

Thus, the solution to this problem is found by iterating the following Algebraic Riccati Equation (ARE) and matrix equations

$$A^T P_n + P_n A + Q - P_n B R^{-1} B^T P_n + \frac{1}{\gamma^2} P_n D D^T P_n + L_n^T R^{-1} L_n = 0 \quad (4.5)$$

$$K_{n+1} = R^{-1} (B^T P_n + L_n) C^T (C C^T)^{-1} \quad (4.6)$$

$$L_{n+1} = R K_{n+1} C - B^T P_n \quad (4.7)$$

until the matrix  $K$  converges to within a desired tolerance.

The two sets of gains, inner loop gains  $K_{in}$  and outer loop gains  $K_{out}$ , were found using this method. The inner loop is defined by the following system

$$\begin{aligned} \dot{\mathbf{x}}_{in} &= A_{in} \mathbf{x}_{in} + B_{in} \mathbf{u} + D_{in} \mathbf{d} \\ \mathbf{y}_{in} &= C_{in} \mathbf{x}_{in} \end{aligned} \quad (4.8)$$

where the states are  $\mathbf{x}_{in} = [\phi, \theta, u, v, w, p, q, r]^T$ , the control inputs are  $\mathbf{u} = [\delta_{lat},$

$\delta_{lon}, \delta_{thr}, \delta_{yaw}]^T$  and the following matrix definitions are given:

$$A_{in} = \begin{bmatrix} 0 & 0 & 0 & 0 & 0 & \Phi_p & 0 & 0 \\ 0 & 0 & 0 & 0 & 0 & 0 & \Theta_q & 0 \\ 0 & X_\theta & X_u & 0 & 0 & 0 & 0 & 0 \\ Y_\phi & 0 & 0 & Y_v & 0 & 0 & 0 & -u_{ref} \\ 0 & 0 & 0 & 0 & Z_w & 0 & u_{ref} & 0 \\ L_\phi & 0 & 0 & 0 & 0 & L_p & 0 & 0 \\ 0 & M_\theta & 0 & 0 & 0 & 0 & M_q & 0 \\ 0 & 0 & 0 & 0 & 0 & 0 & 0 & N_r \end{bmatrix}$$

$$B_{in} = \begin{bmatrix} \Phi_{lat} & 0 & 0 & 0 \\ 0 & \Theta_{lon} & 0 & 0 \\ 0 & 0 & 0 & 0 \\ 0 & 0 & 0 & 0 \\ 0 & 0 & 0 & Z_{thr} \\ L_{lat} & 0 & 0 & 0 \\ 0 & M_{lon} & 0 & 0 \\ 0 & 0 & N_{yaw} & 0 \end{bmatrix}, \quad D_{in} = \begin{bmatrix} 0 \\ I_{6 \times 6} \end{bmatrix}$$

The inner loop is a stabilization control loop which controls the attitude states roll and pitch, as well as all three attitude rates. Therefore, the outputs are  $\mathbf{y}_{in} = [\phi,$

$\theta, p, q, r]^T$  and the output matrix is given as

$$C_{in} = \begin{bmatrix} 1 & 0 & 0 & 0 & 0 & 0 & 0 & 0 \\ 0 & 1 & 0 & 0 & 0 & 0 & 0 & 0 \\ 0 & 0 & 0 & 0 & 0 & 1 & 0 & 0 \\ 0 & 0 & 0 & 0 & 0 & 0 & 1 & 0 \\ 0 & 0 & 0 & 0 & 0 & 0 & 0 & 1 \end{bmatrix}$$

The performance matrices were chosen as  $Q = \text{diag}\{200, 200, 0.2, 0.2, 0.2, 0.01, 0.01, 0.01\}$  and  $R = I_{4 \times 4}$ . Using Eqns. (4.5) through (4.7) the following gain matrix was selected with the values for the gains presented in Table 4.1.

$$K_{in} = \begin{bmatrix} K_{\phi, \delta_{lat}} & 0 & K_{p, \delta_{lat}} & 0 & K_{r, \delta_{lat}} \\ 0 & K_{\theta, \delta_{lon}} & 0 & K_{q, \delta_{lon}} & 0 \\ 0 & K_{\theta, \delta_{thr}} & 0 & K_{q, \delta_{thr}} & 0 \\ K_{\phi, \delta_{yaw}} & 0 & K_{p, \delta_{yaw}} & 0 & K_{r, \delta_{yaw}} \end{bmatrix} \quad (4.9)$$

In order to meet the objective of trajectory tracking, it is imperative to add an outer tracking loop. The variables to be controlled in the outer loop are the positions  $x, y, z$ , the translational velocities,  $u, v, w$ , and the yaw angle  $\psi$ . The outer loop gains are found by first closing the inner loop and augmenting the system by adding the

position and yaw states. The inner closed loop plant is given as

$$\dot{\mathbf{x}}_{\text{in}} = A_{\text{in},CL}\mathbf{x}_{\text{in}} + B_{\text{in}}\mathbf{u} \quad (4.10)$$

$$\mathbf{y}_{\text{in}} = C_{\text{in}}\mathbf{x}_{\text{in}} \quad (4.11)$$

where  $A_{\text{in},CL} = A_{\text{in}} - B_{\text{in}}K_{\text{in}}C_{\text{in}}$  is the inner closed loop system matrix. Augmenting this system with the position and yaw states yields

$$\begin{bmatrix} \dot{\mathbf{x}}_{\text{in}} \\ \dot{x} \\ \dot{y} \\ \dot{z} \\ \dot{\psi} \end{bmatrix} = \begin{bmatrix} A_{\text{in},CL} & 0 \\ & A_A \end{bmatrix} \begin{bmatrix} \mathbf{x}_{\text{in}} \\ x \\ y \\ z \\ \psi \end{bmatrix} + \begin{bmatrix} B_{\text{in}} \\ B_A \end{bmatrix} \mathbf{u} = A_O\mathbf{x}_O + B_O\mathbf{u} \quad (4.12)$$

$$\mathbf{y}_O = C_O\mathbf{x}_O = [x, y, z, u, v, w, \psi]^T \quad (4.13)$$

where  $A_A$  and  $B_A$  describe the linearized model for position and yaw orientation,

$$A_A = \begin{bmatrix} 0 & 0 & 1 & 0 & 0 & 0 & 0 & 0 & 0 & 0 & 0 \\ 0 & 0 & 0 & 1 & 0 & 0 & 0 & 0 & 0 & 0 & u_{ref} \\ 0 & -u_{ref} & 0 & 0 & 1 & 0 & 0 & 0 & 0 & 0 & 0 \\ 0 & 0 & 0 & 0 & 0 & 0 & 0 & \Psi_r & 0 & 0 & 0 \end{bmatrix}, \quad B_A = \begin{bmatrix} 0 & 0 & 0 & 0 \\ 0 & 0 & 0 & 0 \\ 0 & 0 & 0 & 0 \\ 0 & 0 & 0 & \Psi_{yaw} \end{bmatrix}.$$

Eqns (4.5) through (4.7) were again employed to find the outer loop gains where the outer loop performance matrices are chosen as  $Q = \text{diag}\{0.5, 0.5, 1, 1, 1, 0.01,$

0.01, 0.01, 10, 5, 2, 1} and  $R = I_{4 \times 4}$ . The outer loop gain matrix has the structure presented in Eqn (4.14) with the values for the gains listed in Table 4.1.

$$K_{out} = \begin{bmatrix} 0 & K_{y,\delta_{lat}} & 0 & 0 & K_{v,\delta_{lat}} & 0 & K_{\psi,\delta_{lat}} \\ K_{x,\delta_{lon}} & 0 & K_{z,\delta_{lon}} & K_{u,\delta_{lon}} & 0 & K_{w,\delta_{lon}} & 0 \\ K_{x,\delta_{thr}} & 0 & K_{z,\delta_{thr}} & K_{u,\delta_{thr}} & 0 & K_{w,\delta_{thr}} & 0 \\ 0 & K_{y,\delta_{yaw}} & 0 & 0 & K_{v,\delta_{yaw}} & 0 & K_{\psi,\delta_{yaw}} \end{bmatrix} \quad (4.14)$$

## 4.2 State Feedback

As the reader will notice, the inner and outer loop gain matrices are uncoupled and all 12 states are fed-back. Thus, Fig. 4.2 can be equated to the system in Fig.

Table 4.1:  $H_\infty$  Inner Loop and Outer Loop Gains

	Lateral	Longitudinal	Throttle	Yaw
Inner Loop	$K_{\phi,\delta_{lat}} = 13.1322$ $K_{p,\delta_{lat}} = 1.2094$ $K_{r,\delta_{lat}} = -0.1998$	$K_{\theta,\delta_{lon}} = 12.8486$ $K_{q,\delta_{lon}} = 1.3041$	$K_{\theta,\delta_{thr}} = 0.0286$ $K_{q,\delta_{thr}} = -0.0219$	$K_{\phi,\delta_{yaw}} = -1.0306$ $K_{p,\delta_{yaw}} = -0.0554$ $K_{r,\delta_{yaw}} = 0.6329$
Outer Loop	$K_{y,\delta_{lat}} = 5.4088$ $K_{\psi,\delta_{lat}} = 8.7270$ $K_{v,\delta_{lat}} = 6.3502$	$K_{x,\delta_{lon}} = -5.9488$ $K_{z,\delta_{lon}} = 0.0002$ $K_{u,\delta_{lon}} = -5.1979$ $K_{w,\delta_{lon}} = 0.0006$	$K_{x,\delta_{thr}} = 0.1219$ $K_{z,\delta_{thr}} = -1.4701$ $K_{u,\delta_{thr}} = 0.1353$ $K_{w,\delta_{thr}} = -1.0043$	$K_{y,\delta_{yaw}} = 0.3753$ $K_{\psi,\delta_{yaw}} = 2.5480$ $K_{v,\delta_{yaw}} = 0.4888$

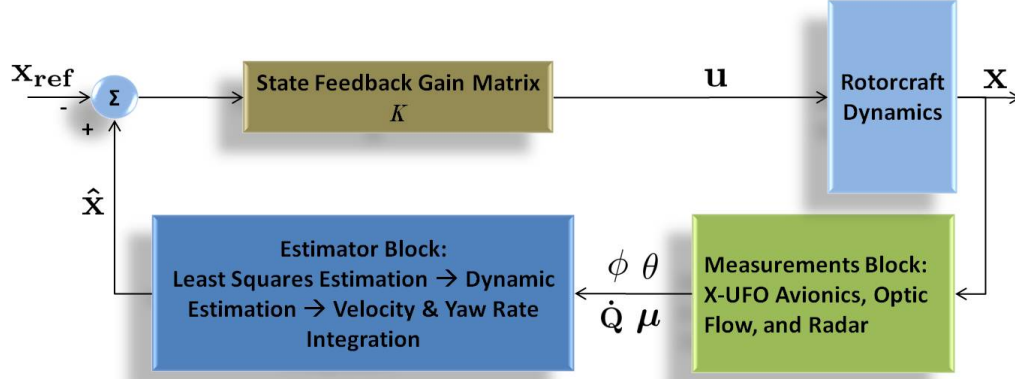


Figure 4.4: Equivalent Control Loop Structure.

4.4 and the system dynamics can be written as

$$\dot{\mathbf{x}} = \begin{bmatrix} A_{in} & 0 \\ A_A \end{bmatrix} \mathbf{x} + \begin{bmatrix} B_{in} \\ B_A \end{bmatrix} \mathbf{u} = A_F \mathbf{x} + B_F \mathbf{u} \quad (4.15)$$

with control law

$$\mathbf{u} = -K(\hat{\mathbf{x}} - \mathbf{x}_{ref}). \quad (4.16)$$

Here,  $\mathbf{x} = [\phi, \theta, u, v, w, p, q, r, x, y, z, \psi]^T$  and the state feedback gain matrix  $K$  is the combination of the inner and outer loop gain matrices  $K_{in}$  and  $K_{out}$ .

$$K = \begin{bmatrix} K_{\phi, \delta_{lat}} & 0 & 0 & K_{v, \delta_{lat}} & 0 & K_{p, \delta_{lat}} & 0 & K_{r, \delta_{lat}} & 0 & K_{y, \delta_{lat}} & 0 & K_{\psi, \delta_{lat}} \\ 0 & K_{\theta, \delta_{lon}} & K_{u, \delta_{lon}} & 0 & K_{w, \delta_{lon}} & 0 & K_{q, \delta_{lon}} & 0 & K_{x, \delta_{lon}} & 0 & K_{z, \delta_{lon}} & 0 \\ 0 & K_{\theta, \delta_{thr}} & K_{u, \delta_{thr}} & 0 & K_{w, \delta_{thr}} & 0 & K_{q, \delta_{thr}} & 0 & K_{x, \delta_{thr}} & 0 & K_{z, \delta_{thr}} & 0 \\ K_{\phi, \delta_{yaw}} & 0 & 0 & K_{v, \delta_{yaw}} & 0 & K_{p, \delta_{yaw}} & 0 & K_{r, \delta_{yaw}} & 0 & K_{y, \delta_{yaw}} & 0 & K_{\psi, \delta_{yaw}} \end{bmatrix} \quad (4.17)$$

The desired reference for the state vector  $\mathbf{x}$ , which allows the vehicle to maintain the desired flight condition of  $u = 1$  m/s by accounting for the pitch and vertical speed variation from hover, is set as

$$\mathbf{x}_{\text{ref}} = [0, -0.0285, 1, 0, -0.0285, 0, 0, 0, x_{\text{ref}}, y_{\text{ref}}, z_{\text{ref}}, \psi_{\text{ref}}]^{\text{T}} \quad (4.18)$$

where  $x_{\text{ref}}$ ,  $y_{\text{ref}}$ ,  $z_{\text{ref}}$ , and  $\psi_{\text{ref}}$  define the trajectory which the vehicle is commanded to track.

## Chapter 5

### MAV Simulation Results

The estimation and navigation methods presented in Chapters 3 and 4 are applied to simulations of a quadrotor vehicle flying through an urban environment, replicating the flight of an autonomous reconnaissance vehicle. This chapter presents the methodology and results obtained from simulation.

#### 5.1 Methodology

The Autonomous Vehicle Laboratory at the University of Maryland developed an in-house simulation environment which provides visualization capabilities as well as the ability to compute optic flow from simulated cameras on robotic platforms. Figure 5.1 depicts scenes from the 3-D simulation environment.

For optic flow estimation, the virtual MAV is equipped with six cameras, each with a  $90^\circ \times 90^\circ$  field of view and a resolution of  $64 \times 64$  pixels. The optic flow cameras cover the six sides of a cube, such that the full spherical viewing arena is imaged. However, for this work, optic flow is only measured on the bottom hemisphere, i.e.  $0 \leq \beta \leq \frac{\pi}{2}$ . In processing the images captured by the optic flow cameras, the imagery is first passed through a Gaussian blurring function to mitigate aliasing issues. A resolution iterative implementation of the Lucas-Kanade algorithm at 60 fps is implemented to calculate optic flow. During flight,  $4N$  image points with

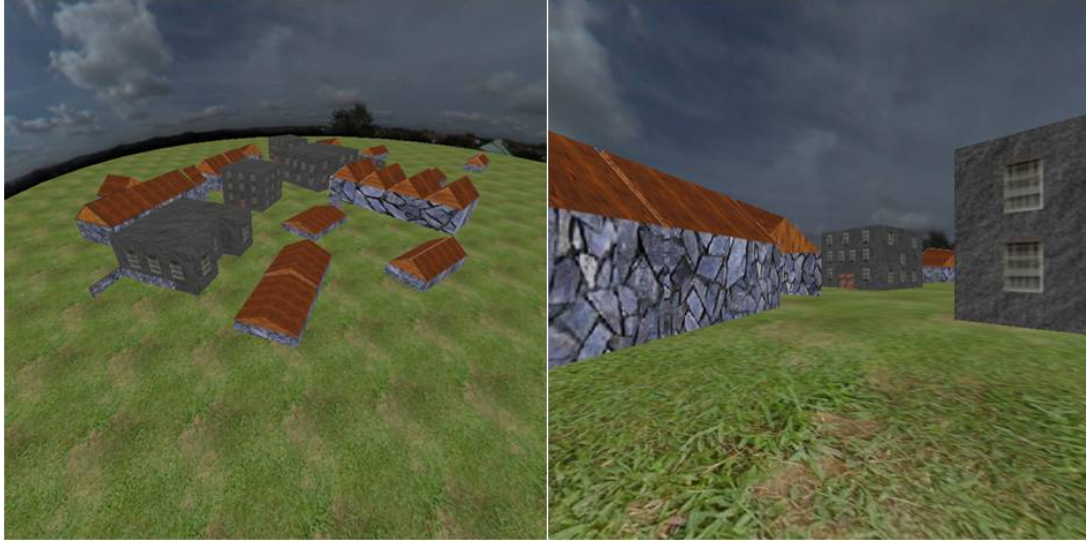


Figure 5.1: 3-D simulation environment.

constant angular spacing along the lower hemisphere of the uv-coordinate spherical grid are tracked. These points are mapped from a virtual sphere surface to the flat cameras via geometric projection. The objects in the simulated environment, including walls, rooftops, the ground and sky, are textured with imagery of sufficient visual contrast so that optic flow can be computed. The optic flow measurements are desampled from  $4N$  to  $N$  by unweighted averaging of square groups of four adjacent nodes. To reduce noise, outlier measurements with a high final cost function or infeasibly large shift estimates are ignored in the block average[22]. This process is summarized in Fig. 5.2. The angular spacing of the optic flow measurement nodes is set to  $9^\circ$ . After the desampling process, the angular spacing of the measurement nodes becomes  $18^\circ$ , which corresponds with the angular spacing of the radar measurement nodes. Figure 5.3 displays a cross section of the quadrotor assuming a sensor field of view encompassing the full lower hemisphere of the viewing surface,

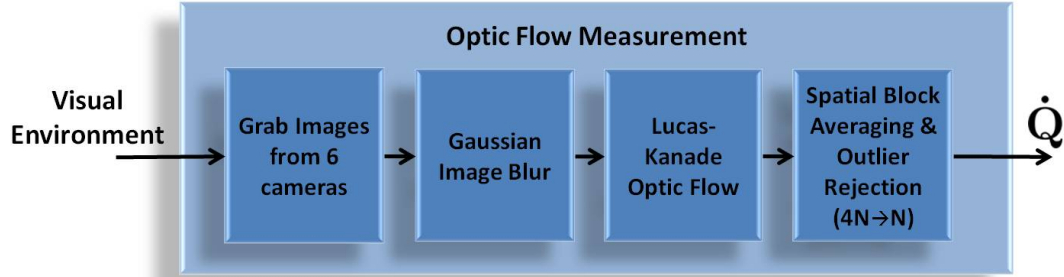


Figure 5.2: Spherical optic flow simulation process diagram.

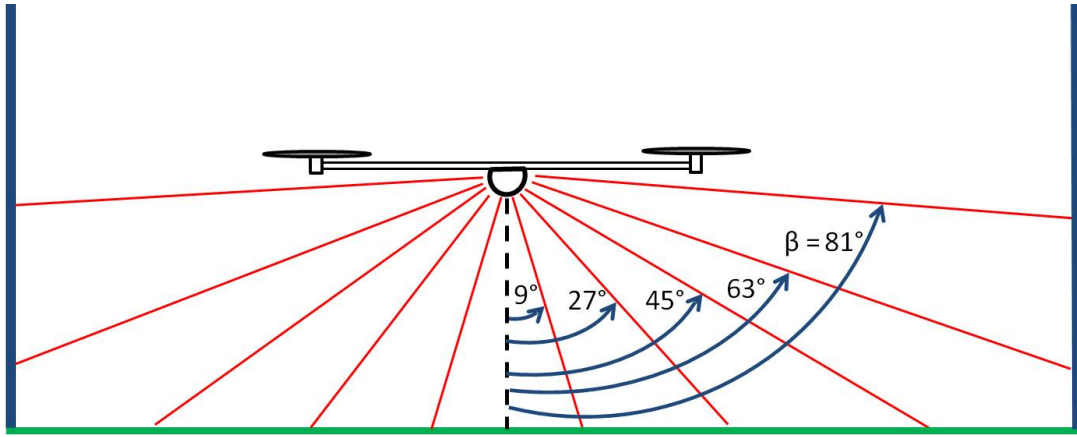


Figure 5.3: Cross sectional view of quadrotor and angular spacing of elevation angle  $\beta$ .

demonstrating the angular spacing of the elevation angle  $\beta$ . After desampling, there are five elevations rings  $\beta = 9^\circ$ ,  $\beta = 27^\circ$ ,  $\beta = 45^\circ$ ,  $\beta = 63^\circ$ , and  $\beta = 81^\circ$  as shown in Fig. 5.3. Each elevation ring contains 20 azimuthal points evenly spaced between  $\gamma = 0^\circ$  and  $\gamma = 360^\circ$ . This angular spacing of the measurement nodes is maintained for all experiments conducted in this work.

## 5.2 Experimental Results

In order to demonstrate both the importance of the FOV and the necessity of a dynamic filter for smaller FOVs, several sensor configurations were simulated. First, the situation of the full lower hemisphere was examined. That is, a FOV of  $180^\circ \times 180^\circ$ , or  $0 \leq \beta \leq \pi/2$ . For this configuration  $N = 100$ . This set-up was tested both with and without the dynamic filtering step.

Next, the FOV was reduced to include just one radar sensor pointing in the  $z_b$  direction, thus a maximum FOV of  $50^\circ \times 30^\circ$ . Referring to Fig. 5.3, it can be seen that, due to the angular spacing of measurement nodes, this FOV encompasses only  $\beta = 9^\circ$ , resulting in an effective FOV of  $18^\circ \times 18^\circ$ . In this configuration  $N = 20$ .

Finally, several simulations were conducted in which the FOV was incrementally reduced from the full lower hemisphere down to just  $18^\circ \times 18^\circ$  in order to determine at what point the dynamic filter step was absolutely necessary to obtain accurate velocity and rate estimates.

### 5.2.1 Measurement Noise Characterization

As discussed in Chapter 3, accurate noise characterization is a crucial step in the Kalman Filtering process. Section 3.3 detailed how the measurement noise was characterized and presented the form of the measurement noise covariance matrix  $R_k$  in Eqn. (3.32). Eqns (5.1) and (5.2) display the values for the covariance matrix  $\Sigma_{\bar{\mathbf{x}}}$  found from the MATLAB<sup>TM</sup> command ‘cov’ for each sensor arrangement. Recall now that the diagonal elements of  $\Sigma_{\bar{\mathbf{x}}}$  are  $\sigma_{\mathbf{v},i}^2$ , the square of the standard deviation

of the  $i^{th}$  element of  $\mathbf{v}$ , and the off-diagonal elements are the covariance between the different noise sources creating  $\mathbf{v}$ . As Eqn (5.2) shows, there is some strong coupling between the noise sources contributing to  $\mathbf{v}$ , which can be expected due to the small field of view and the nature of the least squares estimator which provides  $\hat{\mathbf{x}}_{\text{LS}}$ , as shown in Appendix A.

- Full Lower Hemisphere:

$$\Sigma_{\bar{\mathbf{x}}} = \begin{bmatrix} 0.0026 & 0.0005 & -0.0001 & -0.0001 & -0.0006 & -0.0002 \\ 0.0005 & 0.0029 & 0 & 0.0004 & -0.0001 & -0.0002 \\ -0.0001 & 0 & 0.0010 & 0 & 0.0002 & 0 \\ -0.0001 & 0.0004 & 0 & 0.0008 & 0.0001 & 0 \\ -0.0006 & -0.0001 & 0.0002 & 0.0001 & 0.0019 & 0.0001 \\ -0.0002 & -0.0002 & 0 & 0 & 0.0001 & 0.0006 \end{bmatrix} \quad (5.1)$$

- $18^\circ \times 18^\circ$ :

$$\Sigma_{\bar{\mathbf{x}}} = \begin{bmatrix} 0.6302 & -0.2945 & -0.0697 & -0.1836 & -0.4664 & -0.0337 \\ -0.2945 & 0.9067 & 0.1199 & 0.6440 & 0.1662 & 0.0618 \\ -0.0697 & 0.1199 & 0.0506 & 0.0749 & 0.0399 & 0.0147 \\ -0.1836 & 0.6440 & 0.0749 & 0.4786 & 0.1033 & 0.0377 \\ -0.4664 & 0.1662 & 0.0399 & 0.1033 & 0.3673 & 0.0199 \\ -0.0337 & 0.0618 & 0.0147 & 0.0377 & 0.0199 & 0.0175 \end{bmatrix} \quad (5.2)$$

It is important to note that these  $R_k$  results represent the measurement noise experienced during one 30 second flight. Changes in terrain shapes or image contrast can significantly increase noise in the least squares estimates. Thus,  $R_k$  was manually tuned to improve the filtered state estimates. Since the diagonal elements in  $R_k$  represent the square of the standard deviation of the noise in each velocity and rate estimate, it can be seen from Eqn. (5.1) that the maximum velocity measurement noise standard deviation is about 0.054 m/s while the maximum rate noise standard deviation is about 0.044 rad/s. This suggests that the measurement noise for  $u$ ,  $v$ , and  $w$  will be less than  $3\sigma = 0.162$  m/s for 99% of the time and the measurement noise for  $p$ ,  $q$ , and  $r$  will be less than  $3\sigma = 0.132$  rad/s for 99% of the time. However, it was assumed that more rigorous maneuvers, different terrain shapes and changes in image contrast would increase these standard deviations. Therefore, the standard deviations were rounded up and the diagonal entries of  $R_k$  in (5.1) were each set to  $\sigma^2 = 0.01$ . The diagonal entries in (5.2) were adjusted in a similar fashion, where each entry was set to  $\sigma^2 = 1.0$ .

The results of the experiment conducted to characterize the noise in the full lower hemisphere sensor arrangement also showed the estimated values for  $v$  had a mean error of about -0.31 m/s, while the estimates for the other five states had negligible mean error. This mean error was removed in all analysis of the least squares estimation method, but was not removed from the estimates provided to the Kalman filter.

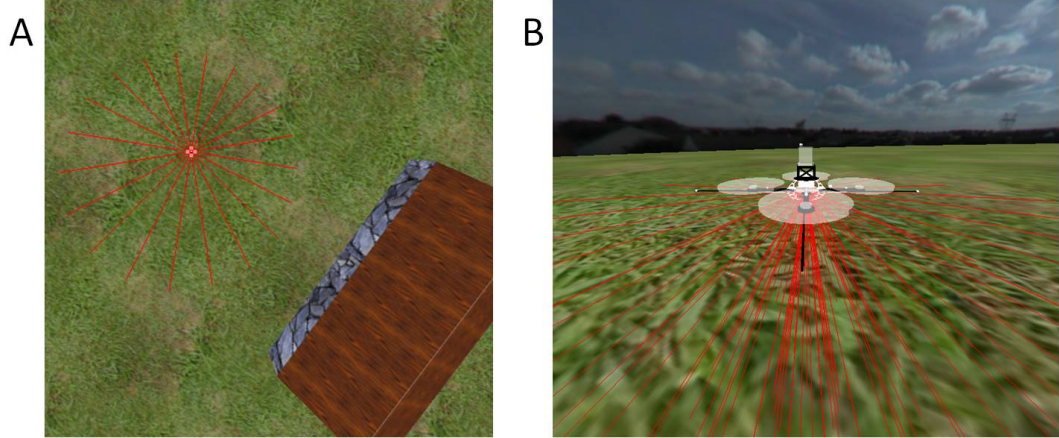


Figure 5.4: Optic Flow and Radar Configuration with a Field of View of the full lower hemisphere. Screen shots from AVLSim of (A) a top view and (B) a rear view.

## 5.2.2 Experiment 1: Full Lower Hemisphere

For the first experimental set-up, the simulated on-board sensors were arranged such that they provided a FOV which encompassed the full lower hemisphere of the spherical imaging surface. That is, a FOV of  $0 \leq \gamma \leq 2\pi$  and  $0 \leq \beta \leq \pi/2$ . Figure 5.4 demonstrates what this sensor arrangement looks like in AVLSim. The red lines emanating from the center of the quadrotor represent the fiducial points  $\mathbf{r}(\gamma, \beta)$  at which optic flow and radar measurements are taken. After the desampling process, measurements are taken at 100 fiducial points, or  $N = 100$ . This set-up was studied both with and without the dynamic filtering step.

### Least Squares Estimation

The case of only a static least squares estimator with a sensor configuration spanning the FOV of the full lower hemisphere was studied in [33]. Figure 5.5 displays a sample of the results obtained using this estimation method. The results

in Fig. 5.5 demonstrate a good match between estimated states and true values, particularly for the pitch rate and heave velocity. The longitudinal and lateral translational velocities, as well as the roll and yaw rates, are also estimated well, but contain some high frequency content which increases the error in these estimates. One simple solution to improve  $\hat{u}$ ,  $\hat{v}$ ,  $\hat{p}$ , and  $\hat{r}$  is to apply a low pass filter to each estimate to smooth the data. Fig. 5.6 demonstrates the impact of applying low pass filters to  $\hat{u}$ ,  $\hat{v}$ ,  $\hat{p}$ , and  $\hat{r}$ . As expected, the filtered estimates have much less high frequency content and provide more accurate knowledge of the longitudinal and lateral velocities and the roll and yaw rates.

## Dynamic Filtering

Instead of applying low pass filters to four of the six estimated states, the Kalman Filtering scheme presented in Chapter 3 was applied. The results of this method can be seen in Fig. 5.7, which presents the data from the same time segment as Figs. 5.5 and 5.6. The data in Fig 5.7 demonstrates improvement over the results in Figs. 5.5 and 5.6. As expected, the Kalman filter more accurately estimates the translational velocities and angular rates than the least squares method and naive low pass filters. Table 5.1 compares the average standard deviations of each rate and velocity estimate for the least squares (LS), low pass filter (LPF), and Kalman filter (KF) estimation schemes.

Figures 5.5, 5.6, 5.7, and Table 5.1 demonstrate that the estimated velocities fit the true values well for each of the respectively implemented state estimation

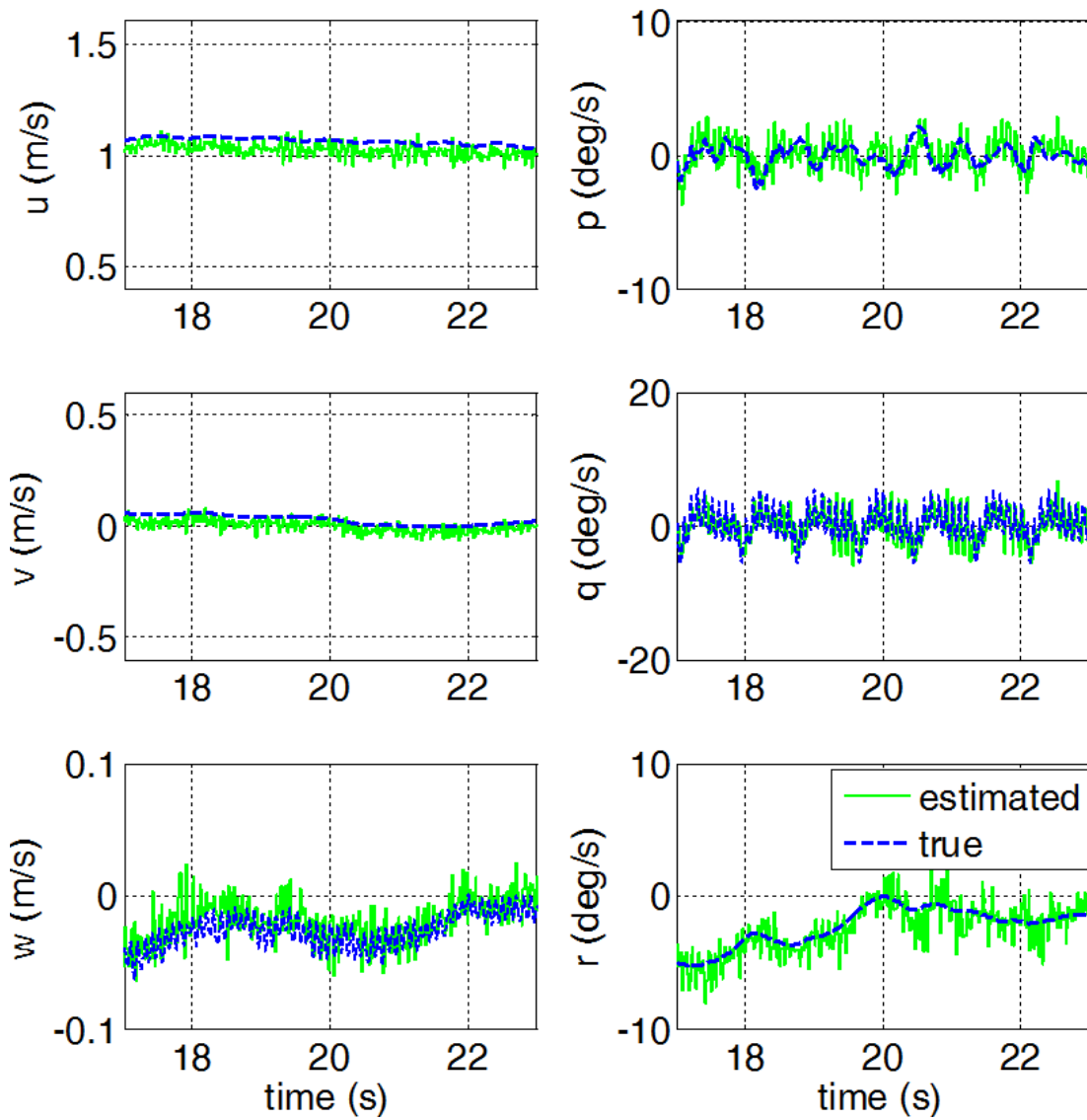


Figure 5.5: Estimated vs. actual speeds and rates with measurements taken over the full lower hemisphere of the viewing surface and estimates found using only the least squares estimation scheme.

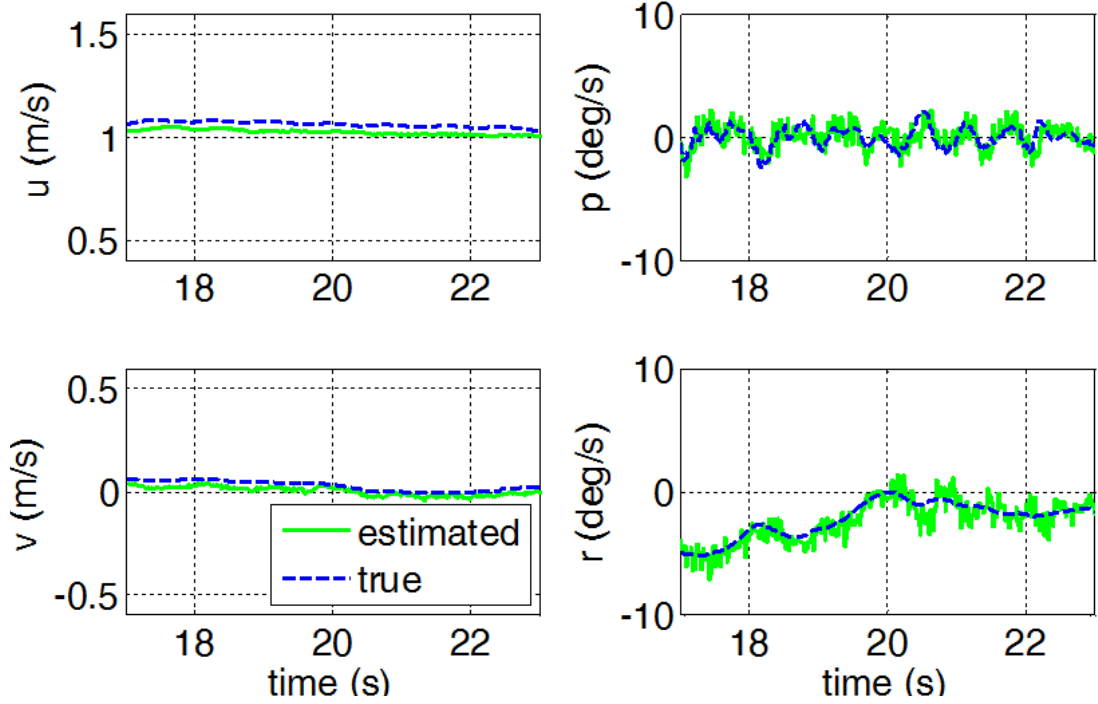


Figure 5.6: Estimated vs. actual speeds and rates with measurements taken over the full lower hemisphere of the viewing surface and estimates found using a low pass filter on the least squares estimates.

schemes. With the wide field of view provided by the sensor arrangement in this case, the least squares estimation scheme generates fairly accurate estimates for all six velocities and rates. The translational velocity estimates  $\hat{u}$  and  $\hat{v}$  and the angular velocity estimate  $\hat{r}$  can be improved greatly with a simple low pass filter due to the low frequency content of each of the three states. In addition, a Kalman Filter can be applied to the estimates provided by the least squares technique to further improve the accuracy of the velocity and rate estimates. However, as seen in Figs. 5.6, 5.7, and Table 5.1, the simple low pass filter is capable of improving  $\hat{u}$  and  $\hat{v}$  about as much as the Kalman filter. The estimate  $\hat{r}$  is improved slightly with a low pass filter, but is improved tremendously by the Kalman filter. It is

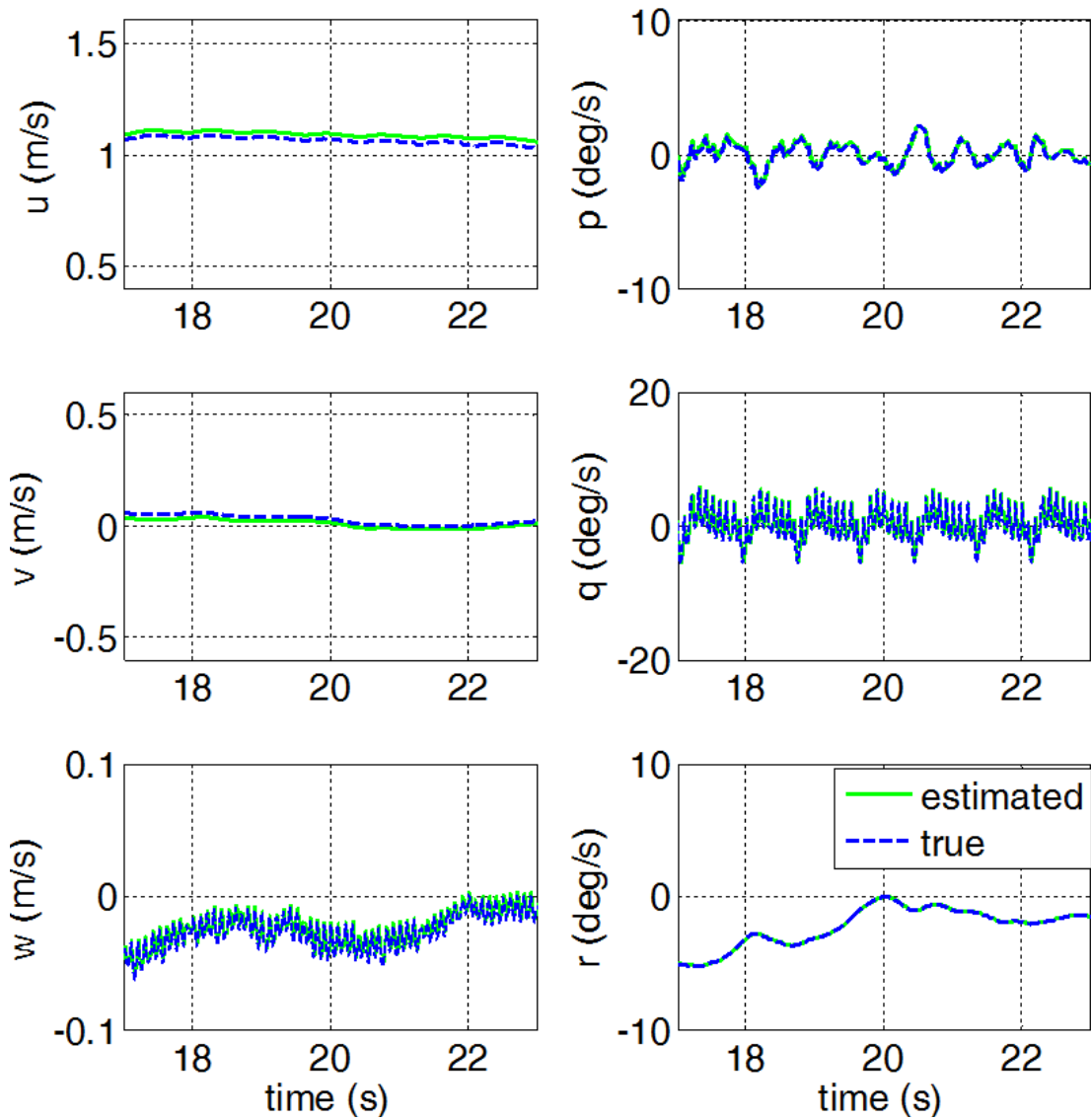


Figure 5.7: Estimated vs. actual speeds and rates with measurements taken over the full lower hemisphere of the viewing surface and estimates found using the Kalman filtering scheme.

Table 5.1: Standard Deviations for Velocity and Rate Estimates

State	Experiment 1			Experiment 2	
	LS	LPF	KF	LS	KF
$u$ (m/s)	0.0360	0.0230	0.0115	0.5396	0.0110
$v$ (m/s)	0.0298	0.0224	0.0191	0.5586	0.0138
$w$ (m/s)	0.0229	—	0.0131	0.0803	0.0131
$p$ (deg/s)	1.4050	1.5247	0.5963	29.1813	0.5960
$q$ (deg/s)	2.3052	—	1.3217	28.7612	1.3223
$r$ (deg/s)	2.2670	2.0230	0.1566	4.3334	0.1358

interesting to note that adding a low pass filter to the least squares estimate for the angular rate  $\hat{p}$  actually causes the standard deviation to increase slightly, indicating that this filtering scheme is somewhat naive in this instance because it worsens the estimates for  $\hat{p}$  rather than improving them. Overall, with the sensor arrangement of Experiment 1, it is best to use the least squares estimation scheme with the addition of low pass filters on  $\hat{u}$ ,  $\hat{v}$  and  $\hat{r}$  because it requires less computation power than the dynamic Kalman filtering scheme. However, the drawback to this scheme is it requires a large field of view which is difficult to obtain with the radar sensor being developed at the Radiation Lab. This arrangement would require several radar sensors which would increase weight and power consumption.

### 5.2.3 Experiment 2: $18^\circ \times 18^\circ$

In an effort to keep weight and power consumption low, a sensor arrangement with a smaller field of view was studied. In Experiment 2, the field of view of the sensors was severely reduced to encompass only a  $50^\circ \times 30^\circ$  area, which corresponds

to the viewing area of one radar sensor, Fig. 5.8. Referring to Fig. 5.3, it can be seen that, due to the angular spacing of measurement nodes, this FOV encompasses only  $\beta = 9^\circ$ , resulting in  $N=20$ . Figure 5.9 displays a sample of data collected using this restricted field of view using only the Least Squares estimation scheme. The figure demonstrates that the estimated values are extremely noisy and do not provide a good knowledge of translational or rotational velocities. Figure 5.10 displays the same section of data after the Kalman Filter in Chapter 3 was applied. Table 5.1 compares the average standard deviations of each rate and velocity estimate for the least squares and Kalman filter estimation schemes.

The results in Fig. 5.9 and Table 5.1 demonstrate that the least squares estimation scheme alone does not provide velocity and rate estimates of sufficient accuracy for this field of view. But the addition of the Kalman Filter not only significantly improves the states estimates, it also increases the accuracy to be com-

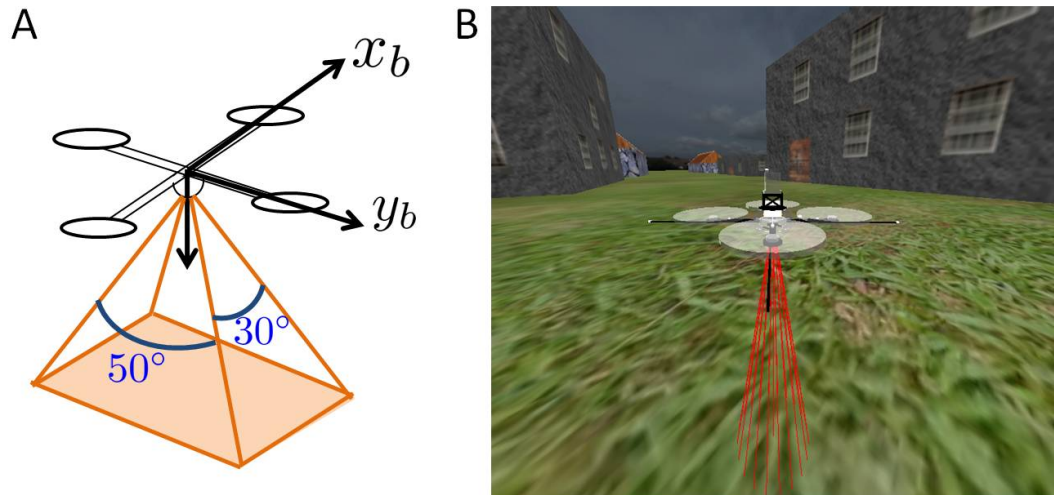


Figure 5.8: Optic Flow and Radar Configuration with a Field of View of  $18^\circ \times 18^\circ$ . (A) Sketch of radar and optic flow sensor capture volume. (B) Screen shot of quadrotor in AVLsim.

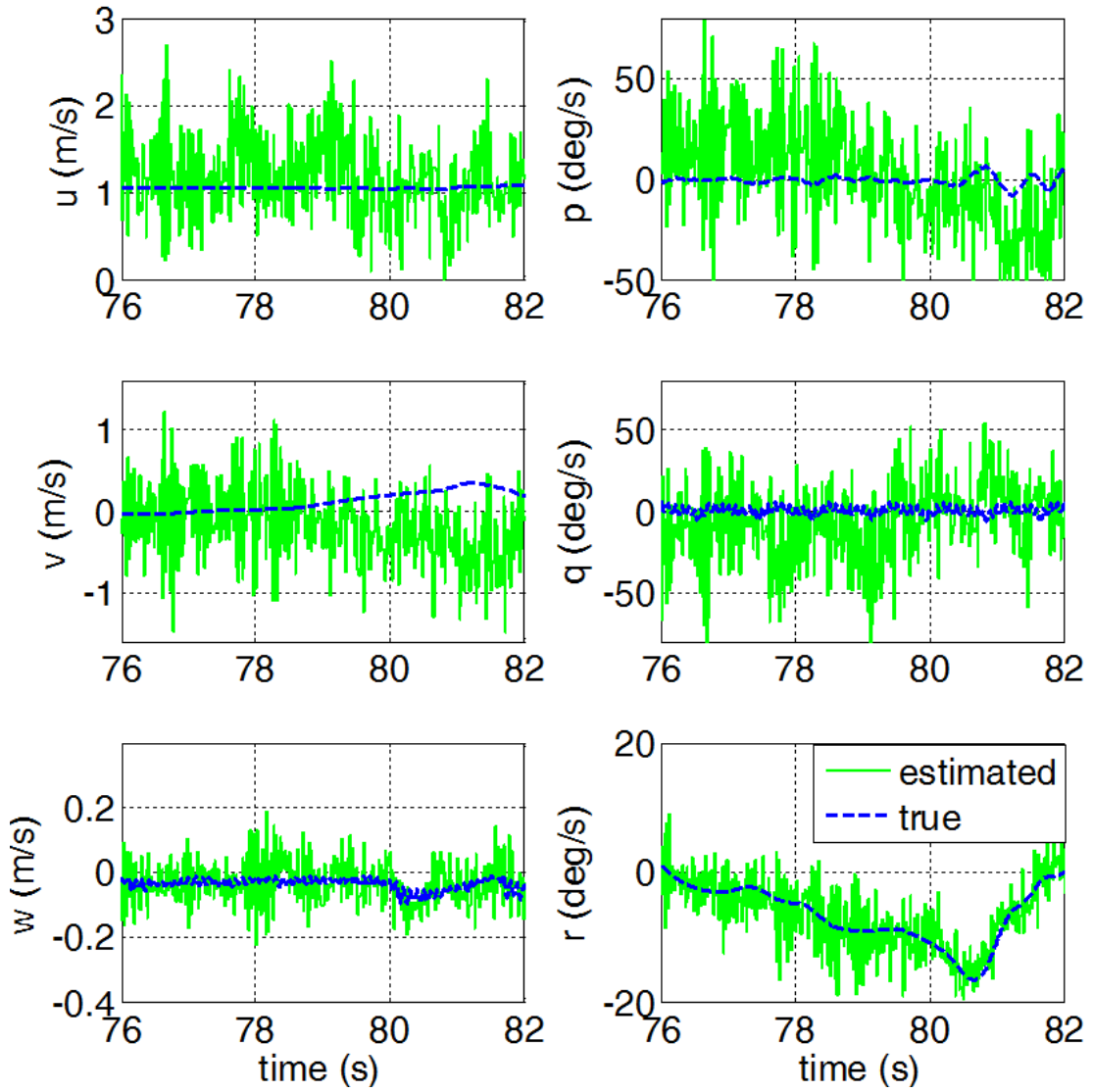


Figure 5.9: Estimated vs. actual speeds and rates with sensor FOV of  $18^\circ \times 18^\circ$  using only the least squares estimation scheme.

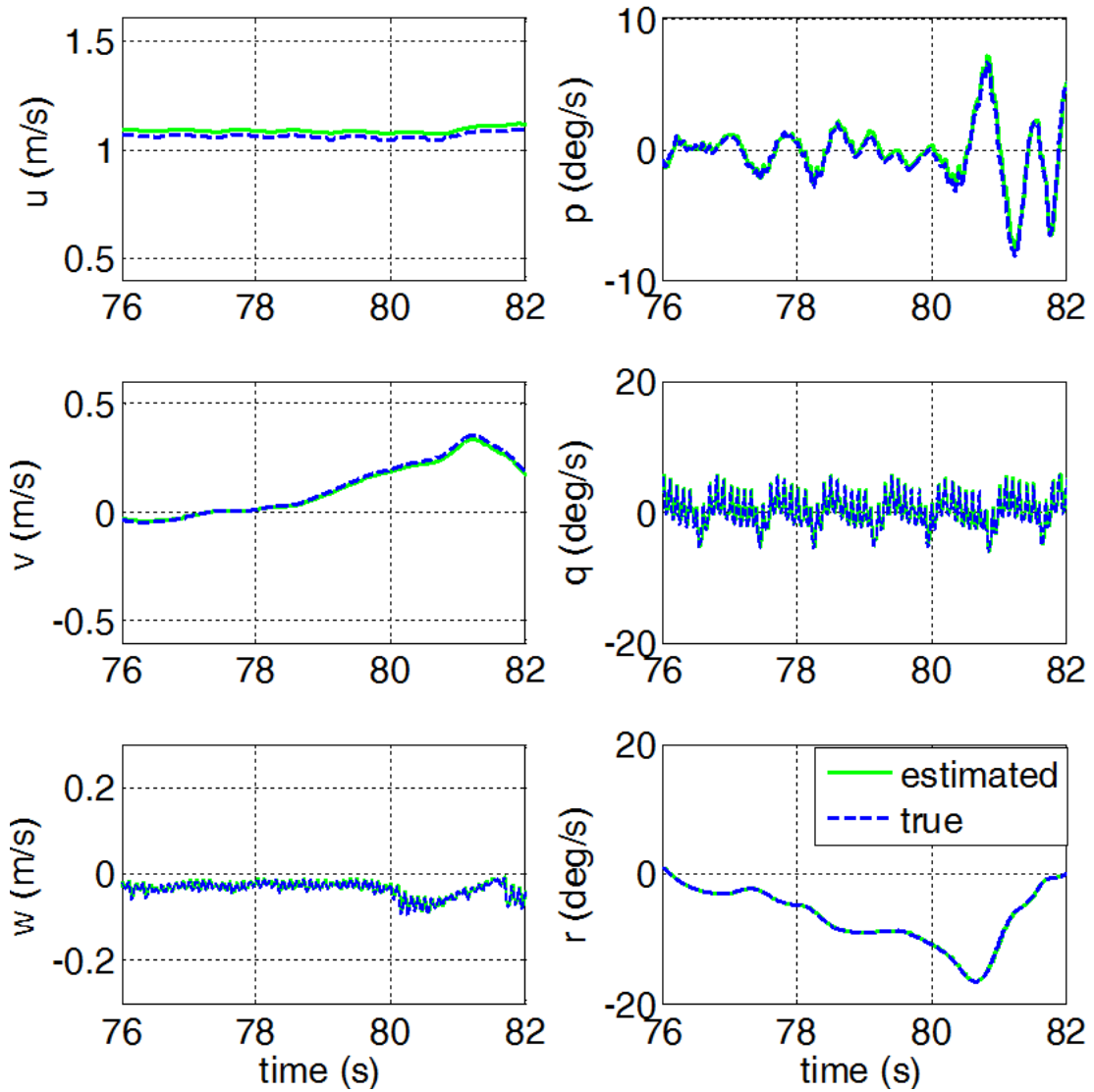


Figure 5.10: Estimated vs. actual speeds and rates with sensor FOV of  $18^\circ \times 18^\circ$  using the Kalman filtering scheme.

parable to, and for some states, better than, the estimates obtained from the wide field of view in Experiment 1.

### 5.3 Discussion

As shown in Section 5.2.2, adequate velocity and angular rate estimates can be obtained with a least squares inversion and simple low pass filter when using a wide field of view. Alternatively, Section 5.2.3 demonstrates a dynamic filter is necessary for obtaining state estimates from a small field of view. As mentioned in Section 5.2.3, the Kalman filter used on the small field of view produced better state estimates, specifically  $\hat{v}$  and  $\hat{r}$ , than the Kalman filter used on the wide field of view sensor arrangement. One simple explanation for this phenomenon is the measurement noise may have been more accurately characterized for the small field of view than the larger field of view. In tuning the measurement noise covariance matrices 5.1 and 5.2, assumptions were made regarding the expected standard deviations for each state which may have been more accurate for Experiment 2 than Experiment 1. It may also be the case that the wide field of view used in Experiment 1 was in fact too large. Both optic flow estimates and radar measurements are distance dependent values whose inaccuracies increase with distance. In the sensor arrangement of Experiment 1, the field of view extends to an angle just below parallel with the vehicle  $x$ - $y$  plane. Since the vehicle's trim position is just slightly askew from parallel with the terrain, the measurements taken at  $\beta = 81^\circ$  can extend off into the horizon if no obstacles are nearby. This can not only increase the distance dependent

noise in the radar measurements, but can also increase the noise in the optic flow measurements since the image contrast can degrade quickly with distance. Thus, measurements taken close to the  $x$ - $y$  plane may not benefit the velocity and rate estimation process, particularly for the states whose motion occurs in the  $x$ - $y$  plane. This theory is tested on two additional experimental sensor configurations.

In order to determine the smallest field of view acceptable for using only the least squares and low pass filter, two more sensor FOVs were tested . Experiment 3 has a field of view of  $0 \leq \beta \leq 45^\circ$  with  $N = 60$  while Experiment 4 has a field of view of  $0 \leq \beta \leq 27^\circ$  with  $N = 40$ . Each of these sensor arrangements were tested on five of the trajectories in Fig. 4.1. Figures 5.11, 5.12, 5.13 and 5.14 display a sample of the results obtained from these experiments and Table 5.2 presents the average standard deviations for the estimates obtained. The results show that the sensor configuration in Experiment 3 yields state estimates whose accuracy is comparable to that of Experiment 1. The state estimates produced via the least squares estimation scheme all tend to be slightly worse in Experiment 3, except for the yaw rate  $\hat{r}$  which is estimated more accurately in Experiment 3. This is particularly interesting since the field of view in Experiment 3 is almost half that of Experiment 1. With the addition of low pass filters, the estimates for  $\hat{u}$  and  $\hat{v}$  improve greatly and have standard deviations very similar to the LPF estimates from Experiment 1. Also, the application of a low pass filter on  $\hat{p}$  improves the estimates in this case, rather than degrading the least squares estimates as in Experiment 1.

The results obtained from Experiment 4 present two interesting phenomena. First, while the smaller field of view causes the estimates for  $\hat{u}$ ,  $\hat{v}$ ,  $\hat{w}$ ,  $\hat{p}$ , and  $\hat{q}$ , to

Table 5.2: Standard Deviations for Velocity and Rate Estimates: Experiments 3 and 4.

State	Experiment 3		Experiment 4	
	LS	LPF	LS	LPF
$u$ (m/s)	0.0500	0.0284	0.1119	0.0360
$v$ (m/s)	0.0401	0.0209	0.1003	0.0342
$w$ (m/s)	0.0260	—	0.0354	—
$p$ (deg/s)	1.7762	1.7074	4.7899	2.6757
$q$ (deg/s)	2.6986	—	5.5405	—
$r$ (deg/s)	0.8193	0.7678	1.6100	0.9855

become even worse than the estimates from Experiments 1 and 3, the estimates for  $\hat{r}$  are still better than those obtained in Experiment 1. Second, while there is a small overall increase in the least squares estimation error between Experiments 1 and 3, which differ by two elevation measurement rings, and slightly larger increase in error between Experiments 3 and 4, which differ by one elevation measurement ring, there is a very substantial increase in estimate error between Experiments 4 and 2, which also only differ by one elevation measurement ring.

Another metric by which the quality of the estimated values is determined is the Frobenius norm. The Frobenius norm is the matrix norm defined as the square root of the sum of the absolute squares of the elements of an  $m \times n$  matrix  $M$  [29]:

$$\|M\|_F = \sqrt{\text{Tr}(M^*M)} \quad (5.3)$$

where  $M^*$  is the complex conjugate of  $M$ . In this usage,  $M$  is defined as the  $6 \times k$  matrix where the elements are the difference between the true and estimated velocity and rate values at each time  $k$ :

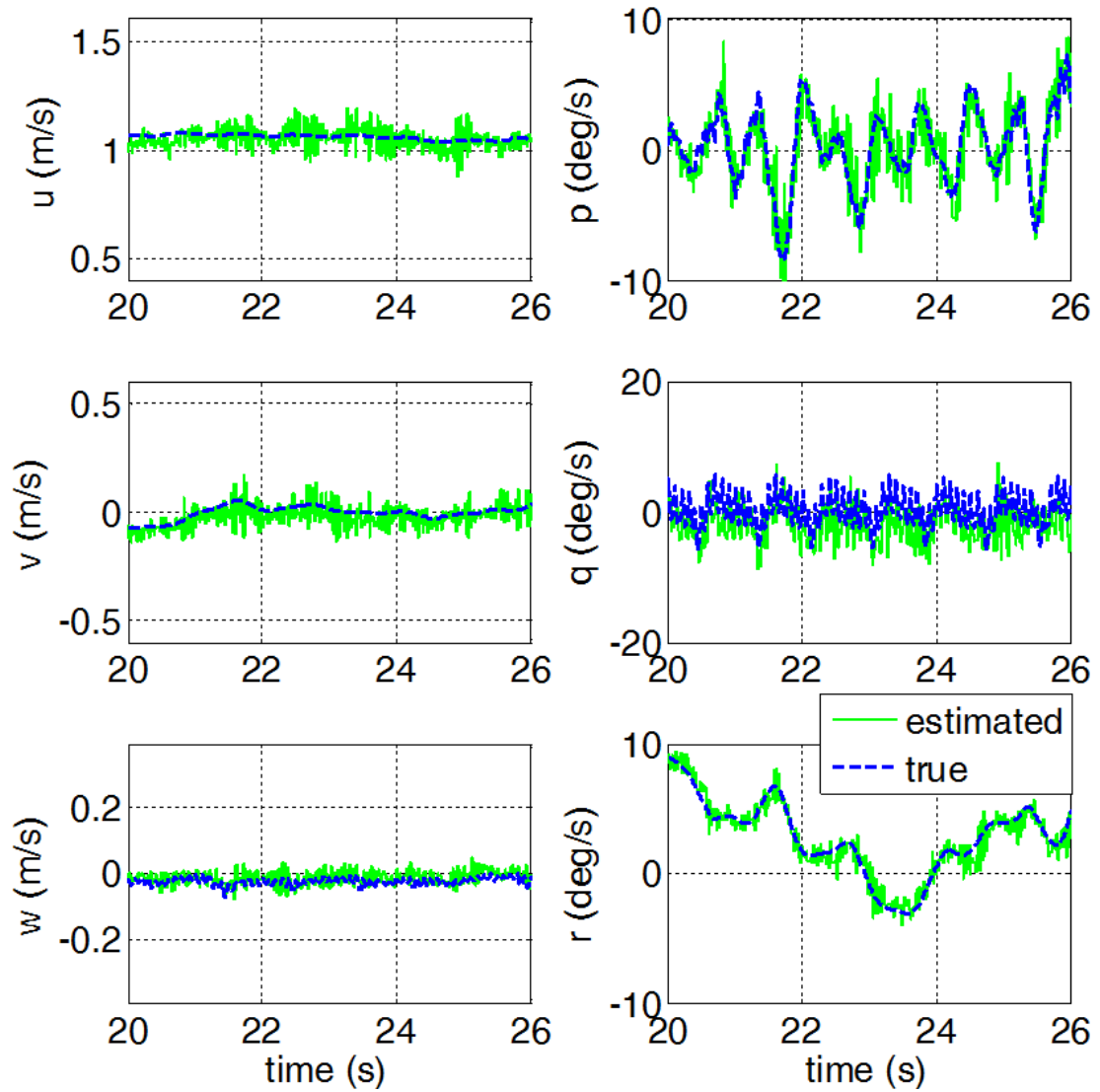


Figure 5.11: Estimated vs. actual speeds and rates with sensor FOV of  $90^\circ \times 90^\circ$  and estimates found using only the least squares estimation scheme.

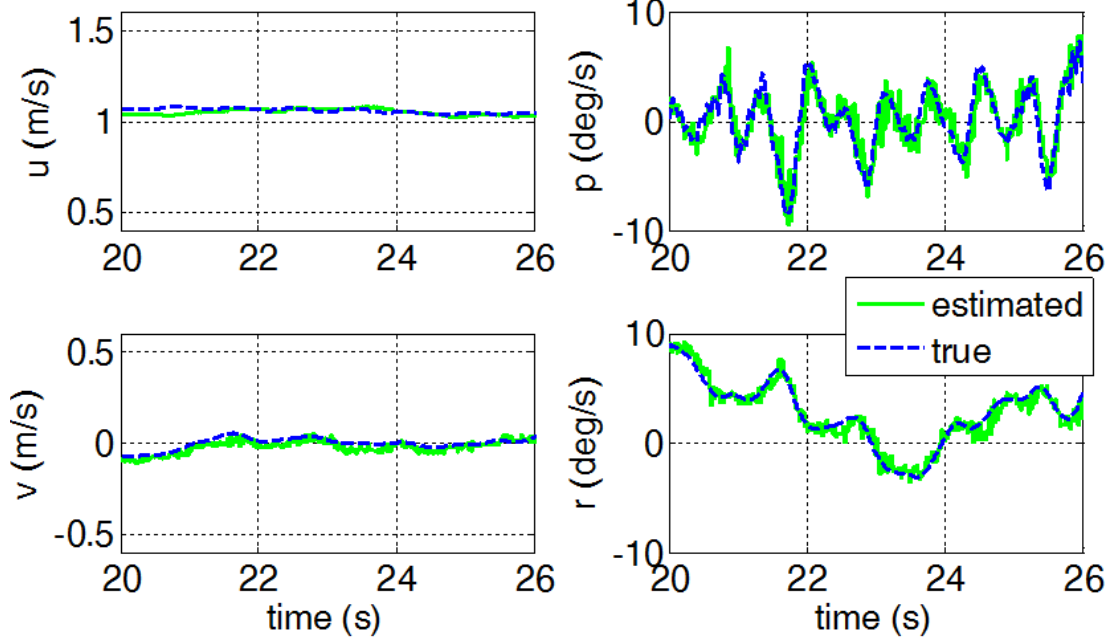


Figure 5.12: Estimated vs. actual speeds and rates with sensor FOV of  $90^\circ \times 90^\circ$  and estimates found using a low pass filter on the least squares estimates.

$$M = \begin{bmatrix} (u_1 - \hat{u}_1) & (u_2 - \hat{u}_2) & \cdots & (u_k - \hat{u}_k) \\ (v_1 - \hat{v}_1) & (v_2 - \hat{v}_2) & \cdots & (v_k - \hat{v}_k) \\ (w_1 - \hat{w}_1) & (w_2 - \hat{w}_2) & \cdots & (w_k - \hat{w}_k) \\ (p_1 - \hat{p}_1) & (p_2 - \hat{p}_2) & \cdots & (p_k - \hat{p}_k) \\ (q_1 - \hat{q}_1) & (q_2 - \hat{q}_2) & \cdots & (q_k - \hat{q}_k) \\ (r_1 - \hat{r}_1) & (r_2 - \hat{r}_2) & \cdots & (r_k - \hat{r}_k) \end{bmatrix}. \quad (5.4)$$

Since the Frobenius norm is single value, it represents the overall goodness of the values estimated for the six translational and rotational velocities. A small value for the Frobenius norm is indicative of a smaller error in the estimates through the full flight. The Frobenius norm for the matrix  $M$  was found for each flight the quadrotor made with each sensor arrangement and estimation technique. Table 5.3

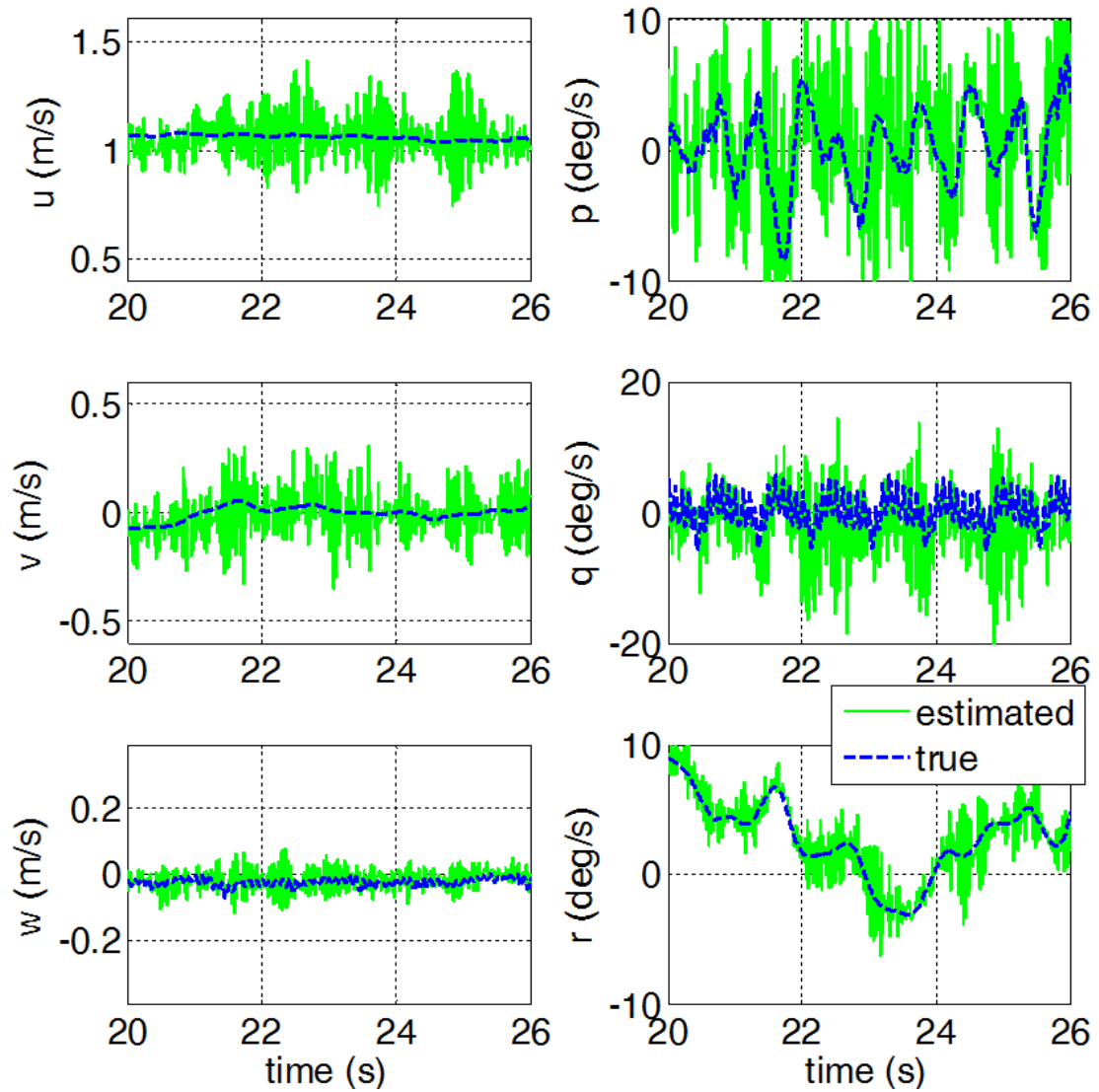


Figure 5.13: Estimated vs. actual speeds and rates with sensor FOV of  $54^\circ \times 54^\circ$  and estimates found using only the least squares estimation scheme.

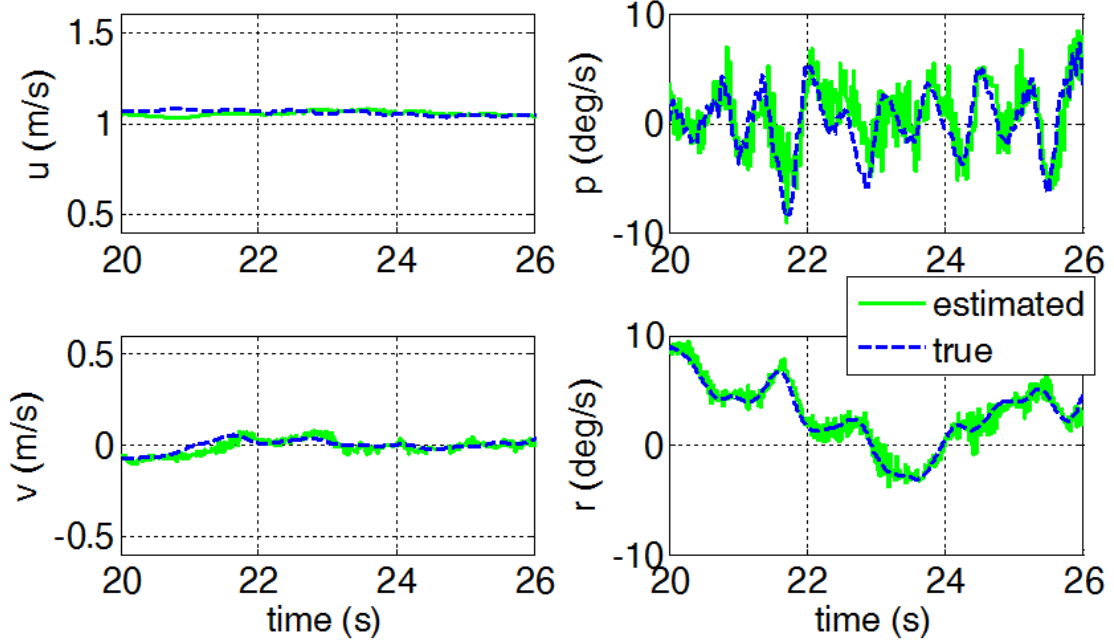


Figure 5.14: Estimated vs. actual speeds and rates with sensor FOV of  $54^\circ \times 54^\circ$  and estimates found using a low pass filter on the least squares estimates.

Table 5.3: Average Frobenius Norm for Velocity and Rate Estimates

Method	Experiment 1	Experiment 2	Experiment 3	Experiment 4
Least Squares	23.3262	287.7601	22.7521	47.0962
Low Pass Filter	21.3925	—	19.1458	30.1584
Kalman Filter	11.2092	10.4819	—	—

presents the average Frobenius norm obtained across all the flights made for each sensor arrangement and estimation scheme.

The results in Table 5.3 further demonstrate that in terms of translational velocity and rotational rate estimation, there is no advantage to using optic flow and radar sensors with an effective field of view larger than a circle of diameter  $90^\circ$ . The results also show that with the addition of a Kalman Filter, the effective sensor field of view does not need to extend beyond a circle of diameter  $18^\circ$  for accurate velocity and rate estimation.

## Chapter 6

### Conclusions and Future Work

This work presents an observer for estimating translational velocities and rotational rates from optic flow and radar measurements. A state feedback control scheme was developed to permit autonomous velocity regulation, vehicle stabilization, and trajectory following for a quadrotor using only the velocity and rate estimates as well as roll and pitch measurements obtained from the built-in avionics package. The results from simulation demonstrate that all the velocity and rate states are estimated accurately. However, particular interest is taken in how well the estimates  $\hat{u}$  and  $\hat{v}$  match the true values. Traditionally, these translational velocities are difficult to measure on MAVs and this work demonstrates a simple and accurate means of doing so. This chapter summarizes the key findings and recommends areas for future work.

#### 6.1 Summary

As discussed in Chapter 1, the primary goal of this work was to determine the feasibility of combining optic flow sensing techniques with radar sensors to obtain accurate estimates for translational and rotational velocities of a 6 DOF micro air vehicle. Towards this end, the theory surrounding optic flow was examined and a method of least squares static estimation was derived using a mathematical model of

2-D optic flow to generate velocity approximations. The estimation scheme was applied to a simulation of a 6 DOF quadrotor vehicle navigating an urban environment. The results illustrated the viability of this estimation scheme by demonstrating an excellent fit to the true velocity values.

Another goal of this work was to determine “optimal” sensor arrangements which allow accurate state estimates to be obtained while also considering the feasibility of hardware implementation. Therefore, various fields of view were studied and the following conclusions were drawn. The results presented in Section 5.3 demonstrate the ability to obtain accurate state estimates with a least squares inversion and simple low pass filter when using a FOV of  $90^\circ \times 90^\circ$  pointing in the positive  $z_b$  direction, i.e. towards the ground. Alternatively, a very restricted field of view, e.g.  $18^\circ \times 18^\circ$ , can be used to obtain accurate velocity and rate estimates with the caveat of an additional dynamic filtering step, such as the Kalman filter presented in Chapter 3.

## 6.2 Limitations of Applicability

While the work described here provides an exciting and novel method of state estimation in addition to an effective feedback control scheme, there are some issues which limit the applicability of these algorithms as implemented here. First, from Appendix A, it can be seen that the measurement noise covariance matrix is state dependent. That is,  $\Sigma_{\bar{x}}$  depends on  $u$ ,  $v$ , and  $w$  which appear in the matrix  $S$ . This occurs because of the method by which the optic flow and radar measurements

are combined. As shown in (2.3) and (3.10) optic flow is a function of the radar measurements, and thus also a function of the noise in the radar measurements, which results in the noise  $\boldsymbol{\eta}$  being multiplied by the states  $u$ ,  $v$ , and  $w$ . This suggests that a rigorous analysis of the measurement noise covariance matrix would need to make certain assumptions about the environment.

Second, as seen in (2.4), the linearized attitude kinematics of the quadrotor vehicle used in this study have control terms. That is,  $\dot{\phi}$ ,  $\dot{\theta}$ , and  $\dot{\psi}$  include the terms  $\Phi_{lat}$ ,  $\Theta_{lon}$ , and  $\Psi_{yaw}$  which are control derivatives. While counter-intuitive, the reader is reminded that the equations of motion for this vehicle were obtained from a previous study in which system identification techniques suggested these terms fit an input/output relationship. This does not mean the terms necessarily exist, but instead were just found to fit the linear model and most likely appear in the model due to the quadrotor's built-in inner stabilization control loop.

Third, there are a few limitations to the implementation of optic flow on real systems. Optic flow requires a certain amount of visual contrast to provide good measurements. If the imaged environment has poor contrast, such as a room with white walls and floor, the optic flow measurements will be poor as a result of uniformity in the pixel images. Also, optic flow is dependent on luminosity, i.e. the relative brightness of the environment. Therefore, optic flow measurements will be poor if the vehicle is in a dark or foggy environment.

### 6.3 Future Work

The observer was implemented in simulation and has proven to be a valid method of state estimation. However, experimental tests should be conducted to demonstrate the work presented here as a feasible, practical and realistic approach to MAV velocity and rate estimation. To this end, the obstacle which must be overcome is hardware feasibility. For optic sensing, the field of view requirements can be met easily by a single downward pointing camera. For obtaining distance measurements, the FOV requirement of  $18^\circ \times 18^\circ$  can easily be attained by a single radar sensor. The additional requirement of a dynamic filtering scheme with this field of view will unfortunately increase the on-board processing requirement, but should be feasible on MAVs such as the quadrotor studied in this work. However, the reader will note that the system assumed in this work is linear time invariant. Thus, a steady state Kalman Filter can be implemented, in which a time invariant Kalman gain matrix  $L_{ss}$  is found and used for all time  $k$ , resulting in significantly reduced processing requirements. In contrast, the FOV requirement of  $90^\circ \times 90^\circ$  necessitates the use of several radar sensors, or suggests the need for a radar sensor with a larger FOV. However, the benefit of this FOV is that accurate velocity and rate estimates can be obtained with a simple static least squares estimator which requires less computation power than a dynamic estimator, and is therefore more suitable for use on MAVs. Experimental validation of these techniques will soon be possible using the radar sensors under development at the Radiation Laboratory of the University of Michigan. In the meantime however, if a few sonar sensors were

used in place of a radar sensor, it may be possible to reformulate the estimation process with the measurement model presented in (3.9) to obtain estimates for  $\hat{u}$ ,  $\hat{v}$ , and  $\hat{r}$ , with the additional caveat that the quadrotor be constrained to 3 DOF. Such an experiment would further prove the feasibility of velocity estimation techniques presented here.

Next, the work presented in this thesis derived a feedback control scheme suitable for velocity regulation, vehicle stabilization, and trajectory following. Ideally, however, the vehicle would be able to autonomously navigate an unmapped environment without following a prescribed trajectory. Thus, while this work provides an excellent means of partial state estimation, it ignores the problem of obstacle detection and avoidance. Future work should address this problem by taking further advantage of the radar sensors. In this case, two radar sensors should be used on-board the vehicle — one would be used for small field of view velocity and rate estimation, while the second could be pointed forward along the  $x_b$ -axis and be used as a means of simultaneous localization and mapping to provide the vehicle with pose and yaw estimates  $\hat{x}$ ,  $\hat{y}$ ,  $\hat{z}$ ,  $\hat{\psi}$ . This would allow the vehicle to autonomously navigate a cluttered environment without being constrained to predetermined trajectories.

## Appendix A

### Measurement Noise Derivations

First, from Section 3.3 we know that the measurement noise covariance matrix is given by  $\Sigma_{\bar{\mathbf{x}}} = E[\bar{\mathbf{x}}\bar{\mathbf{x}}^\top] = E[(\hat{\mathbf{x}}_{\text{LS}} - \mathbf{x}_v)(\hat{\mathbf{x}}_{\text{LS}} - \mathbf{x}_v)^\top]$ . Next, recall that  $\hat{\mathbf{x}}_{\text{LS}} = (H^\top H)^{-1}H^\top \tilde{\mathbf{z}}$ . Thus,

$$\Sigma_{\bar{\mathbf{x}}} = E[((H^\top H)^{-1}H^\top \tilde{\mathbf{z}} - \mathbf{x}_v)((H^\top H)^{-1}H^\top \tilde{\mathbf{z}} - \mathbf{x}_v)^\top] \quad (\text{A.1})$$

Now define

$$H^\dagger \equiv (H^\top H)^{-1}H^\top \quad (\text{A.2})$$

Note that although  $H$  is a time-varying matrix, it is still a deterministic matrix, thus  $H^\dagger$  is also deterministic. If we substitute  $\tilde{\mathbf{z}}$  with Eqn. (3.5) we get

$$\Sigma_{\bar{\mathbf{x}}} = E[(H^\dagger H \mathbf{x}_v + H^\dagger \mathbf{v} - \mathbf{x}_v)(H^\dagger H \mathbf{x}_v + H^\dagger \mathbf{v} - \mathbf{x}_v)^\top] \quad (\text{A.3})$$

$$= E[(\mathbf{x}_v + H^\dagger \mathbf{v} - \mathbf{x}_v)(\mathbf{x}_v + H^\dagger \mathbf{v} - \mathbf{x}_v)^\top] \quad (\text{A.4})$$

$$= E[(H^\dagger \mathbf{v})(H^\dagger \mathbf{v})^\top] \quad (\text{A.5})$$

$$= E[H^\dagger \mathbf{v} \mathbf{v}^\top (H^\dagger)^\top] \quad (\text{A.6})$$

$$= H^\dagger E[\mathbf{v} \mathbf{v}^\top] (H^\dagger)^\top \quad (\text{A.7})$$

Next, recall from Section 3.1.1.2 that  $\mathbf{v}$  is the combination of the optic flow measurement noise  $\boldsymbol{\nu}$  and the nearness measurement noise  $\boldsymbol{\eta}$ ,

$$\mathbf{v} = \begin{bmatrix} \mathbf{v}_\gamma \\ \mathbf{v}_\beta \end{bmatrix} = \begin{bmatrix} \nu_{\gamma,1} + \eta_1(u \sin \gamma_1 - v \cos \gamma_1) \\ \vdots \\ \nu_{\gamma,N} + \eta_N(u \sin \gamma_N - v \cos \gamma_N) \\ \nu_{\beta,1} + \eta_1(-u \cos \beta_1 \cos \gamma_1 - v \cos \beta_1 \sin \gamma_1 + w \sin \beta_1) \\ \vdots \\ \nu_{\beta,N} + \eta_N(-u \cos \beta_N \cos \gamma_N - v \cos \beta_N \sin \gamma_N + w \sin \beta_N) \end{bmatrix}$$

If we set  $\mathbf{v} = \boldsymbol{\nu} + S\boldsymbol{\eta}$  where  $S$  is the  $2N \times 2N$  deterministic diagonal matrix  $S = \text{diag}\{(u \sin \gamma_1 - v \cos \gamma_1), \dots, (u \sin \gamma_N - v \cos \gamma_N), (-u \cos \beta_1 \cos \gamma_1 - v \cos \beta_1 \sin \gamma_1 + w \sin \beta_1), \dots, (-u \cos \beta_N \cos \gamma_N - v \cos \beta_N \sin \gamma_N + w \sin \beta_N)\}$ , then we can write

$$\Sigma_{\bar{\mathbf{x}}} = H^\dagger E[(\boldsymbol{\nu} + S\boldsymbol{\eta})(\boldsymbol{\nu} + S\boldsymbol{\eta})^\top](H^\dagger)^\top \quad (\text{A.8})$$

$$= H^\dagger (E[(\boldsymbol{\nu}\boldsymbol{\nu}^\top)] + SE[\boldsymbol{\eta}\boldsymbol{\eta}^\top]S^\top + E[\boldsymbol{\nu}\boldsymbol{\eta}^\top]S^\top + S^\top E[\boldsymbol{\eta}\boldsymbol{\nu}^\top])(H^\dagger)^\top \quad (\text{A.9})$$

Since the optic flow measurement noise is uncorrelated with the radar measurement noise,  $E[\boldsymbol{\nu}\boldsymbol{\eta}^\top] = E[\boldsymbol{\eta}\boldsymbol{\nu}^\top] = 0$  and

$$\Sigma_{\bar{\mathbf{x}}} = H^\dagger (E[(\boldsymbol{\nu}\boldsymbol{\nu}^\top)] + SE[\boldsymbol{\eta}\boldsymbol{\eta}^\top]S^\top)(H^\dagger)^\top \quad (\text{A.10})$$

$$= H^\dagger (\sigma_\nu^2 I + S\sigma_\eta^2 S^\top)(H^\dagger)^\top \quad (\text{A.11})$$

$$= H^\dagger (\sigma_\nu^2 I + \sigma_\eta^2 S S^\top)(H^\dagger)^\top \quad (\text{A.12})$$

This results in a  $6 \times 6$  matrix which is not strictly diagonal due to the  $H^\dagger$  terms. In other words, noise in the different “measured” states may be coupled even though the optic flow noise and radar noise are uncorrelated with themselves or each other.

## Bibliography

- [1] K. Sarabandi, M. Vahidpour, M. Moallem, and J. East. “Compact Beam Scanning 240GHz Radar for Navigation and Collision Avoidance,” Proc. SPIE 8031, 803113 (2011).
- [2] L. Pierce, J.S. Humbert, S. Gerardi, K. Sarabandi, and M. Moallem. “Combined radar and Optical Flow Navigation for Flying Robots in Urban Areas,” International Symposium on Antennas and Propagation and UNSC/USRI National Radio Science Meeting, July 2011.
- [3] S. Hrabar and G.S. Sukhatme. “Omnidirectional Vision for an Autonomous Helicopter,” IEEE International Conference on Robotics and Automation, 558-563 (2003) .
- [4] T. Webb and R. Prazenica. “Vision-Based State Estimation for Autonomous Micro Air Vehicles,” Journal of Guidance, Control, and Dynamics, Vol 30, No 3, 816-826 (2007).
- [5] Seung-Min Oh and Eric N. Johnson. “Relative Motion Estimation for Vision-based Formation Flight using Unscented Kalman Filter,” AIAA Guidance, Navigation, and Control Conference (2007).
- [6] O. Toupet, J. D. Paduano, R. Panish, R. Sedwick, and E. Frazzoli. “Augmenting state estimates with multiple camera visual measurements.” In Proceedings of the AIAA Infotech@Aerospace Conference and Exhibit. AIAA-2007-2983, Rohnert Park, CA, 2007.
- [7] Jacob Willem Langelaan. *State Estimation for Autonomous Flight in Cluttered Environments*. PhD Thesis, Stanford University, 2006.
- [8] Laurent Muratet, Stephane Doncieux, Yves Briere, and Jean-Arcady Meyer. A contribution to vision-based autonomous helicopter flight in urban environments. *Elsevier Science*, 2004.
- [9] J. Santos-Victor, G. Sandini, F. Curroto, and S. Garibaldi. Divergent stereo in autonomous navigation - from bees to robots. *International Journal of Computer Vision*, 14:159-177, 1995.
- [10] M. V. Srinivasan, J.S. Chahal, K. Weber, S. Venkatesh, M.G. Nagle and S.W. Zhang. Robot navigation inspired by principles of insect vision. *Robotics and Autonomous Systems*, 26:203-216, 1999.

- [11] Chris McCarthy and Nick Barnes. “Performance of Optical Flow Techniques for Indoor Navigation with a Mobile Robot.” Proc. IEEE International Conference on Robotics and Automation (2004).
- [12] A. Argyros, D. Tsakiris, and C. Groyer. Biomimetic centering behavior for mobile robots with panoramic sensors. *IEEE Robotics and Automation Magazine*, pages 21-30, December 2004.
- [13] J. Serres, F. Ruffier, and N. Franceschini. Two optic Flow regulators for speed control and obstacle avoidance. *In Proceedings of the IEEE International Conference on Medical Robotics and Biomechatronics*. Pisa, Italy, February, 2005.
- [14] A. Beyeler, J. Zufferey, and D. Floreano. “3D Vision-based Navigation for Indoor Microflyers,” Proc. IEEE International Conference on Robotics and Automation (2007).
- [15] S. Zingg, D. Scaramuzza, S. Weiss, and R. Siegwart. “MAV Navigation through Indoor Corridors Using Optical Flow,” Proc. IEEE International Conference on Robotics and Automation (2010).
- [16] P. Gurfil and H. Rotstein. “Partial Aircraft State Estimation from Visual Motion Using the Subspace Constraints Approach,” *Journal of Guidance, Control, and Dynamics*, Vol 24, No 5, 1061-1028 (2001).
- [17] Joseph J. Kehoe, Adam S. Watkins, Ryan S. Causey, and Rick Lind. “State Estimation using Optical Flow from Parallax-Weighted Feature Tracking,” AIAA Guidance, Navigation, and Control Conference (2006).
- [18] F. Kendoul, I. Fantoni, and K. Nonami. “Optic flow-based vision system for autonomous 3D localization and control of small aerial vehicles,” *Robotics and Autonomous Systems* 57, 591-602 (2009).
- [19] J. S. Humbert, R. M. Murray, and M. H. Dickinson. “Pitch-Altitude Control and Terrain Following Based on Bio-Inspired Visuomotor Convergence,” AIAA Guidance, Navigation, and Control Conference (2005).
- [20] J. Sean Humbert. *Bio-Inspired Visuomotor Convergence in Navigation and Flight Control Systems*. PhD Thesis, California Institute of Technology, 2005.
- [21] J. Conroy, G. Gremillion, B. Ranganathan, J. S. Humbert. “Implementation of wide-field integration of optic flow for autonomous quadrotor navigation,” *Autonomous Robots* Vol. 27, No. 3, 189-198 (2009).

- [22] A. Hyslop and J. S. Humbert. “Autonomous Navigation in Three-Dimensional Urban Environments Using Wide-Field Integration of Optic Flow,” *Journal of Guidance, Control, and Dynamics*, Vol 33, No 1, 147-159 (2010).
- [23] Andrew Hyslop. *Bio-Inspired Information Extraction in 3-D Environments Using Wide-Field Integration of Optic Flow*. PhD Thesis, University of Maryland, College Park, 2010.
- [24] M. O. Franz, J. S. Chahl, and H. G. Krapp. “Insect-Inspired Estimation of Egomotion,” In *Neural Computation*, Vol. 16, Issue 11, November 2004, pp 2245 - 2260.
- [25] J. J. Koenderink and A. J. van Doorn. Facts on optic flow. *Biol. Cybern.*, 56(4):247-254, 1987.
- [26] G. Gremillion and J. S. Humbert. “System Identification of a Quadrotor Micro Air Vehicle,” *AIAA Conference on Atmospheric Flight Mechanics* (2010).
- [27] A. Singh. *Optic Flow: A Unified Perspective*, IEEE Computer Society Press, Los Alamitos, CA (1991).
- [28] E. P. Simoncelli, E. A. Adelson, and D. J. Heeger. “Probability distributions of optic flow,” *Conference on Computer Vision and Pattern Recognition* (1991).
- [29] John L. Crassidis and John L. Junkins. *Optimal Estimation of Dynamic Systems*. Chapman & Hall/CRC, Boca Raton, FL, 2004.
- [30] Robert G. Brown and Patrick Y.C. Hwang. *Introduction to Random Signals and Applied Kalman Filtering*. John Wiley and Sons, New York, 1992.
- [31] Arthur Gelb. *Applied Optimal Estimation*. The M.I.T. Press, 1974.
- [32] Jyotirmay Gadewadikar, Frank L. Lewis and Murad Abu-Khalaf. “Necessary and Sufficient Conditions for  $H_\infty$  Static Output-Feedback Control,” *Journal of Guidance, Control, and Dynamics*, Vol 29, No 4, 915-920 (2006).
- [33] S. Gerardi, J.S. Humbert, L. Pierce, and K. Sarabandi. “Velocity Estimation Using Optic Flow and Radar,” *Proc. SPIE 8031*, 803112 (2011).